UNIVERSIDADE DE SÃO PAULO
INSTITUTO DE FÍSICA DE SÃO CARLOS

HUGO RODRIGUES DAMASCENO

Solid-state NMR on the quadrupolar low-γ nucleus ^{25}Mg: Application to glasses

São Carlos
2023

HUGO RODRIGUES DAMASCENO

Solid-state NMR on the quadrupolar low-γ nucleus ^{25}Mg: Application to glasses

Dissertation presented to the Graduate Program in Physics at the Instituto de Física de São Carlos, Universidade de São Paulo, to obtain the degree of Master of Science.

Area of concentration: Theoretical and Experimental Physics
Advisor:
Prof. Dr. Hellmut Eckert

Corrected Version

(Original version available on the Program Unit)

São Carlos
2023

Damasceno, Hugo Rodrigues
Solid-state NMR on the quadrupolar low-gamma nucleus 25Mg: Application to Glasses / Hugo Rodrigues Damasceno; advisor Hellmut Eckert; co-advisor Marcos de Oliveira Junior - corrected version -- São Carlos 2023.
78 p.

Dissertation (Master's degree - Graduate Program in Theoretical and Experimental Physics) -- Instituto de Física de São Carlos, Universidade de São Paulo - Brasil , 2023.

1. Magnesium. 2. Glass. 3. Aluminosilicate. 4. NMR. 5. Silicate. I. Eckert, Hellmut, advisor. II. de Oliveira Junior, Marcos, co-advisor. III. Title.

With love,
to my parents

ACKNOWLEDGEMENTS

I am deeply grateful to Professor Hellmut Eckert for offering me the chance to join his research group and for his unwavering support and guidance throughout my studies. I would also like to express my appreciation to my co-advisor, Marcos de Oliveira Junior, for his invaluable contributions to my academic growth.

I would like to extend my sincerest thanks to Millena Lograd, Bianca Cerrute, Henrik Bradtmüller, Anuraag Gaddam, and Igor Silva for their delightful company during coffee breaks and for enriching NMR discussions that were so instrumental to my progress.

I am greatly appreciative of the financial support provided by Conselho Nacional de Desenvolvimento Científico e Tecnológico (CNPq) and Nippon, which helped me complete my Master's degree.

I am eternally grateful to my loving family - my parents Paulo and Edvânia, my brother Pedro, and my grandmother Eva - for their unwavering love and support, which sustained me through even the most challenging times.

I would also like to express my heartfelt gratitude to my girlfriend and partner, Droanna, who inspired me to push past my self-imposed limits and reach new heights.

Last but not least, I would like to thank all of my friends and relatives who have been a part of my journey and have helped shape me into the person I am today. Thank you for your support and encouragement.

"*Science is the best model of knowledge we have, and we should strive to improve it constantly. But we need to remember that all science is based on assumptions, and that it is always possible that we discover something new that changes everything we thought we knew.*"

- Yuval Noah Harari,
Sapiens: A Brief History of Humankind (2014)

ABSTRACT

DAMASCENO, H. R. **Solid-state NMR on the quadrupolar low-γ nucleus ^{25}Mg:** application to glasses. 2023. 78 p. Dissertation (Master in Science) – Instituto de Física de São Carlos, Universidade de São Paulo, São Carlos, 2023.

In the present work, the structure of magnesium alumino and aluminosilicate glasses were studied using several techniques of Solid State NMR. The study employed high magnetic field strengths and fast magic angle spinning to address the structural organization of the glasses. The utility of dipolar spin echo decay and static ultrawide line NMR (WURST) was tested on isotopically enriched ^{25}Mg samples to extract information about the relevant interactions concerning the ^{25}Mg nuclei. The results of the study were complemented by additional static and high-resolution ^{27}Al and ^{29}Si NMR techniques, which addressed the structural organization of the silicate and alumosilicate networks surrounding the magnesium ions. The ^{29}Si MAS NMR spectroscopy was employed for the study, but due to limitations in the amount of material available and long spin-lattice relaxation times, reliable signal deconvolution was not obtained. The spectra were found to be consistent with previously published data, but the study found that the average isotropic chemical shifts and full widths at half maximum were found to be identical for the samples with and without ^{25}Mg isotopic enrichment for MAS 226 glass, with stronger deviations for the other compositions. The ^{27}Al MAS-NMR results suggest the presence of two distinct aluminum coordination environments in the samples and a small fraction of six-coordinated aluminum in the sample iso MAS 25. The findings were further validated by complementary techniques such as ^{27}Al MQMAS NMR spectra and SATRAS-NMR. All these results form the basis of a comprehensive description of the local structure of magnesium silicate and alumosilicate glasses.

Keywords: Magnesium. Glass. NMR. Aluminosilicate. Silicate.

RESUMO

DAMASCENO, H. R. **RMN do estado sólido no núcleo quadrupolar de baixo-γ ^{25}Mg:** aplicação em vidros. 2023. 78 p. Dissertação (Mestre in Ciências) – Instituto de Física de São Carlos, Universidade de São Paulo, São Carlos, 2023.

No presente trabalho, a estrutura amostras de vidros de alumínio e aluminossilicato de magnésio foram estudadas usando várias técnicas de RNM de Estado Sólido. O estudo empregou altos campos magnéticos e MAS-NMR para estudar a organização estrutural dos vidros. Medida de spin echo decay e WURST foi testada em amostras enriquecidas com o isótopo ^{25}Mg para obter informações sobre as interações relevantes a cerca do núcleo ^{25}Mg. Os resultados obtidos foram complementados por métodos adicionais de RMN estático e de alta resolução para os núcleos ^{27}Al e ^{29}Si, onde a estrutura das redes silicatadas e aluminossilicatadas em torno dos íons de magnésio foram estudadas. O MAS-RMN sobre ^{29}Si foi realizada no estudo, mas devido às limitações devido pouca quantidade de material disponível e aos longos tempos de relaxamento spin-rede, não foi obtido uma desconvolução de sinal confiável. Os espectros se mostraram consistentes com dados previamente publicados, mas o presente estudo descobriu que os desvios químicos isotrópicos médios e as larguras a meia altura foram idênticos para as amostras com e sem enriquecimento de ^{25}Mg para o vidro MAS 226 e com desvios mais fortes para outras composições. Os resultados RMN sobre núcleo ^{27}Al com técnica MAS sugerem a presença de dois ambientes de coordenação de alumínio distintos nas amostras e uma pequena fração de alumínio 6 coordenado na amostra iso MAS 25. Esses resultados foram ainda validados por técnicas complementares, como os espectros de NMR sobre o núcleo ^{27}Al com as técnicas MQMAS e SATRAS-NMR. Esses resultados formam uma base descritiva abrangente da estrutura local de vidros de silicato e aluminossilicato de magnésio.

Palavras-chave: Magnésio. Vidros. RMN. Aluminosilicato. Silicato.

LIST OF FIGURES

LIST OF TABLES

CONTENTS

1 INTRODUCTION

Solid-state Nuclear Magnetic Resonance (NMR) is one of the most powerful techniques to assess structure for many different materials. NMR spectroscopy presents an excellent capability to differentiate between atoms on crystallographically inequivalent sites in a quantitative fashion, which makes the method very useful to confirm proposed structure models from X-ray diffraction by comparing signal intensities with predicted site multiplicities. For example, is possible to validate the proposed crystal structure further and check its quality by comparing the nuclear electric quadrupolar coupling constants and asymmetry parameters computed directly from the crystal structure data with those measured using NMR spectroscopy. The ability of NMR to resolve locally distinct environments allows an in-depth characterization of order/disorder phenomena including: 1) occupancy deficiencies in non-stoichiometric compounds, 2) site multiplicities produced by positional disordering, and 3) superstructure formation, polymorphism, and phase transitions.

Even nowadays, NMR spectroscopy continues to expand in many science fields such as physics, chemistry, biology, medicine, and material science. The increasing range of NMR techniques is employed for either spectroscopic studies or imaging purposes, much of it becoming possible because of the high magnetic fields created by superconducting solenoids, and the availability of fast computers for controlling the timing of pulse sequences, the acquisition of experimental data and algorithms of data processing. These improvements together with the realization of fast sample spinning and accurately timed pulse sequences have led to the present state of the art of high-resolution solid-state nuclear magnetic resonance. As result of this evolution, the number of publications concerning applied structural studies in the material science has been continuously increasing since the 1980's.

In the present work we study the application of some techniques which allow to overcome difficulties affecting the NMR characterization of the relatively low-receptive magnesium isotope ^{25}Mg, which is an insensitive NMR-active isotope featuring low natural abundance (10%), featuring a nuclear spin quantum number of 5/2, and relatively large nuclear electric quadrupole moment $Q = +1.99 \cdot 10^{-29}$ m^2, and a rather low gyromagnetic ratio of $\gamma = 1.639 \cdot 10^7$ s^{-1} T^{-1}.

The importance of studying Mg comes from the fact that it is a critical element in

the solid-state science of many technologically important materials. Mg is a well-known additive in oxide glasses, enhancing their crack resistance and mechanical stability (1), and modifying their bioactive properties. (2) The structural role of Mg in glasses has been subject to some controversy. While some authors consider Mg as a regular network modifier, other studies view it to be integrated in the network as doubly charged MgO_4^{2-} species. Also, the coordination number is a matter of on-going debate, where four (3 - 4), five (5) and six (6) have been proposed.

For glasses, which only present short- or medium range order, but not the long-range order, NMR presents a good study opportunity because it is locally selective, element selective and presents a quantitative character. From the solid-state NMR techniques, it is possible to differentiate the coordination number in a quantitative fashion.

The present dissertation addresses the structural organization of magnesium-containing silicate glasses, via a combination of high magnetic field strengths and fast magic angle spinning. In addition, the utility of dipolar spin echo decay and static ultrawide line NMR are being tested on isotopically enriched specimens, to extract information about the relevant interactions concerning the ^{25}Mg reporter nuclei. The work is complemented by additional static and high-resolution ^{27}Al and ^{29}Si NMR methods, addressing structural organization of the silicate and alumosilicate networks surrounding the magnesium ions. All these results form the basis of a comprehensive description of the local structure of magnesium silicate and alumosilicate glasses.

2 BACKGROUND

The objective of the present section is to elucidate the basic theoretical and conceptual aspects needed to understand the scientific questions addressed in this work.

2.1 OVERVIEW ON GLASSES

While it is possible to find glasses in nature from volcanic origin such as the obsidian, and alumino-silicate glass containing oxides of Na, K, Ca, Fe and traces of Mn, industrial glasses manufacture is a multi-billion dollars industry, and new applications are surrounding human daily life and modern technologies. Additives have been studied with the intent to change the glass properties tailoring them to their application. Differently from other materials, glass properties are determined largely by their chemical composition.

The many applications that range from art to engineering, pose enough motivation for studying composition-structure-property relations in glasses. The structural role of Mg in glass is of special interest in this regard because Mg confers important mechanical, biological and chemical properties on glasses, making it a key ingredient in the compositional optimization of glasses in numerous application fields.

The first question to be addressed from a fundamental point of view, concerns the definition of the term "glass". While a layman can understand glass as a transparent solid sensitive to impact, the scientific definition describes glass as a frozen supercooled liquid that is X-ray amorphous, i.e., lacks long-range order. It is also possible to add the fact that when it is heated, it should also exhibit a thermal characteristic known as the “glass transition” at temperature Tg. From the thermodynamic point of view, we could say that at Tg the quantities related to the Gibbs energy’s second derivative (heat capacity, thermal expansivity and compressibility) undergo abrupt changes as a function of temperature. (7)

It is possible to base a paradigm on the work by Zachariasen (8), later modified by Greaves. (9) Zachariasen’s continuous random network (crn) hypothesis proposed that the atoms in glassy material are continuously connected in a random way in a corner-sharing mode, producing a polymeric structure lacking in periodicity. Later, Greaves proposed the so-called modified random network (MRN) model, which is characterized by percolation paths or channels of structure- modifying components. This second

model explains qualitatively many of the physical and diffusion related properties of silicate glasses. (9) Greaves' model remains influential for providing a qualitative understanding of the structural role for network modifiers.

While glass appears to be a solid if observed on the timescale of macroscopic property measurements, presenting properties such as mechanical rigidity, elasticity, and susceptibility to scratches and fractures, it also presents liquid-like properties such as viscous flow behavior and continuous relaxation towards the supercooled liquid state, tending to crystallize as its ultimate fate. As described by Zanotto (10), glass presents its own state, which is:

> "… a nonequilibrium, non-crystalline condensed state of matter that exhibits a glass transition. The structure of glasses is similar to that of their parent supercooled liquids (SCL), and they spontaneously relax toward the SCL state. Their ultimate fate, in the limit of infinite time, is to crystallize."

2.1.1 THERMODYNAMICS OF GLASSES

Glasses are considered the amorphous solids formed by the supercooling of melts, bypassing the crystallization process, avoiding the nucleation and growth processes that would drive the material towards thermodynamic equilibrium. The required cooling rates therefore are determined by the velocity of crystallization, ν, of the material, which is given by equation (1)

$$\nu = \frac{L(T_m - T)}{3\pi a^3 \eta T_m} \qquad (1)$$

where L is the heat of fusion; a is the typical distance through which the particles must move during the crystallization process, considered to be of the order of the lattice constant; η is the melt viscosity, and Tm is the temperature of the liquid → solid phase transition. Because viscosity increases exponentially during cooling, the velocity of crystallization rapidly decreases after passing a certain critical temperature interval indicated in Figure 2.1.

For an infinitely fast quenching process, the fictive temperature (T_f) is introduced. (11) Because it is not directly measured, it is roughly estimated by the intersection of the extrapolation of the behavior of volume as function of the temperature in the states of supercooled liquid and the glass.

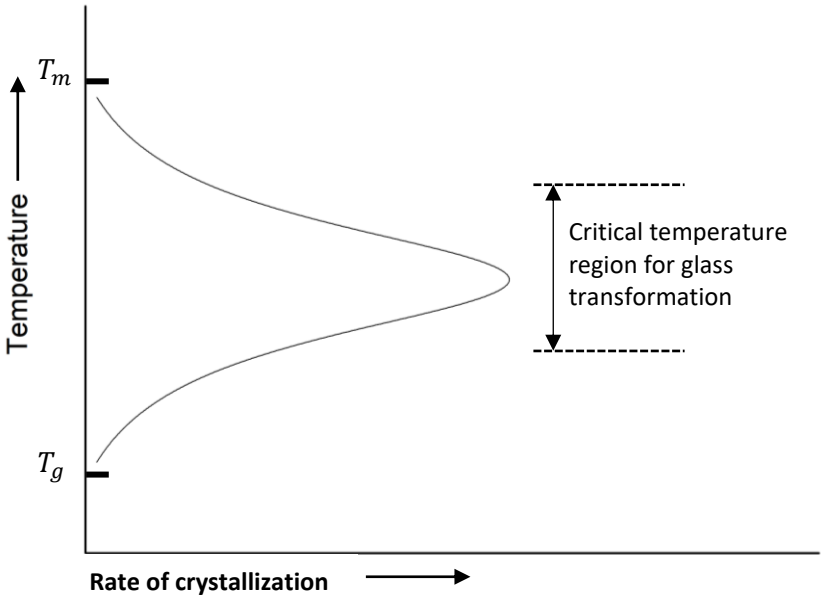

Figure 2.1 - Dependence of rate of crystallization of a supercooled liquid on temperature
Source: RAO. (7)

Although the approach using a distribution of fictive temperatures enjoyed much success in the engineering disciplines, it was shown that the nonequilibrium glassy state is substantially different from the equilibrium liquid state, and for this reason the concept of fictive temperature should not be used by researchers who seek a realistic microscopic description of glass. (12) Therefore, it will be used in this work in its simplest fashion only for didactic purposes, determining the temperature around which the glass transition will be found.

It is possible to foment the discussion about the glass formation based on Figure 2.2, which shows a volume versus temperature diagram, and we use the above cited fictive temperatures (vertical dashed lines in purple and red) to determine the temperatures around which the glass formation from the supercooled liquid to proceed.

For temperatures below the melting temperature Tm, crystallization is suppressed for sufficiently rapid cooling rates. In this case, the system finds itself in the metastable state of the supercooled liquid, and because the viscosity of the system increases rapidly with decreasing temperature, the molecules, or structural fragments (moieties), lose mobility upon. Once temperatures sufficiently low are reached, these units stop rearranging and do not reach the volume characteristic that would correspond to the molar volume of the metastable liquid at that temperature, but rather conserve the excess volume the melt had at or near the glass transition temperature. If the cooling rate is rapid, molar

volume follows the trajectory marked in purple in Figure 2.2, while for slower cooling rates the trajectory marked in red is being followed. (13) Both curves, for fast and slow cooling, are close to parallel to the trajectory followed by the thermodynamically stable crystalline solid. Those trajectories are essentially dominated by the anharmonicity of the vibrational modes encountered in the corresponding vibrational density of states.

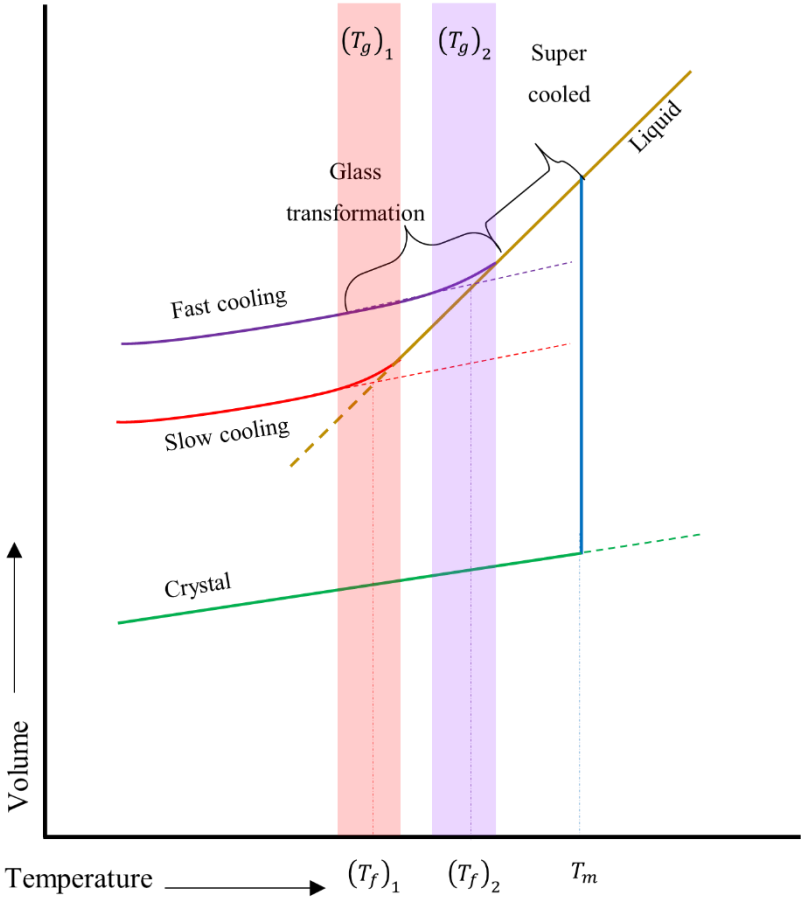

Figure 2.2 - Volume-temperature diagram for a glass-forming liquid.
Source: VARSHNEYA. (13)

2.1.2 ORDER IN GLASS

Multiple experimental investigations have shown that there is no complete absence of order in glasses, but there is a certain amount of residual order in the sub-nanometer region. This is a natural consequence of interatomic interaction potentials which show distinct minima, both with respect to bond lengths and bond angles due to chemical bond formation. In this respect, it is possible to categorize both short-range order (SRO) and medium-range order (MRO).

From Zachariasen's CRN model, glass is defined as an extended network of corner sharing oxygen polyhedral which lacks periodicity, as the local variations in the oxygen-related bond angles induces a loss of translational symmetry/long-range periodicity. Therefore, highly ionic compounds such as MgO and Al_2O_3 are not good glass formers, because the long-range coulombic interactions favor edge- and face sharing, promoting the crystallization of the material.

A different model aims at the idea that glasses are made up of micro, and ultra-micro, crystals, and crystalline regions, no more than few angstroms in size, and separated by amorphous layers. (13) Although this is long known as incorrect, the concept of ultra-microcrystalline regions has continued to receive active consideration in glass science. (14)

Just as in crystals, the primary polyhedral unit remains the same in the glassy state, for the CRN model which define the 'short range order' (SRO). But following the proposed model, it is possible to determines a secondary distance range comprising next-nearest neighbors, which characterizes the connectivity between individual coordination (short-range order unit). This distance region has been called intermediate range order. In certain cases, these motifs form larger structural units such as clusters, chains, or rings, which are identified as "medium range order" motifs. (13 - 14)

Figure 2.3 depicts the structural description of the continuous random network model in relation to the long-range ordered structure of a crystalline material, for a A_2O_3 material in a (A) crystalline and (B) glassy state.

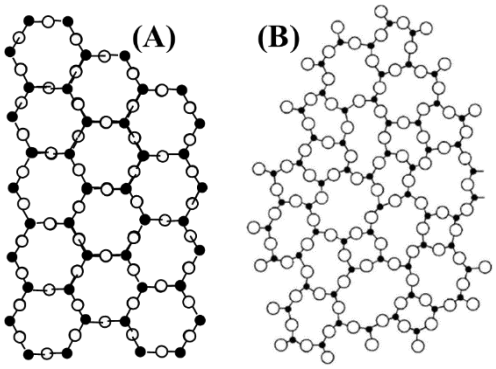

Figure 2.3 - Scheme of the atomic structuralrepresentation.
Source: By the author

2.1.3 GLASS NETWORK FORMERS, MODIFIERS, AND INTERMEDIATE OXIDES.

modifier (NWM). NWFs, being the main species that shape the glass structure, form the backbone of the glass, and contribute to its disordered network. On the other hand, NWMs play a key role by modifying the bonding properties of the NWFs, thus transforming the glass structure into a macro-polyanion. By using these terms, it becomes easier to understand the intricacies of glass structure.

Among the most common NWFs, we can mention SiO_2, B_2O_3 and $P2O_5$, which are of interest of the present work. From Zachariasen's rules, each of these species creates a rigid cation-centered polyhedron, connected by bridges of oxygen at the vertices. While SiO_2 can form a stable glass on its own, with no need of additional components to the network, Al_2O_3 requires charge stabilization by network modifiers in order to form a stable glass network. (13)

As NWMs of interest here and widely used in technology and science, MgO and CaO are generally considered modifiers that convert bridging oxygens to nonbridging oxygens (NBOs), reducing the connectivity of the networks presented in Figure 2.3 (B). The network modifier cations Mg^{2+} and Ca^{2+} are situated in irregular coordination polyhedral mostly defined by non-bridging oxygen species, with which they interact primarily via Coulombic forces. Figure 2.4 summarizes this schematic description of a structural representation of the glass state containing network former and modifiers, and the oxygen atoms are represented by open circles.

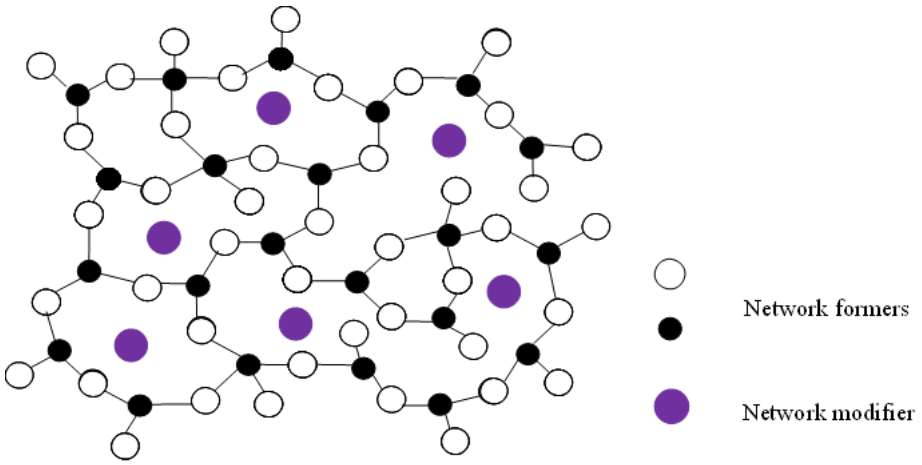

Figure 2.4 - Structural representation of the glass state.
Source: By the author

2.2 BASIC THEORY OF NMR SPECTROSCOPY

Nuclear magnetic resonance (NMR) spectroscopy is based on the magnetism of atomic nuclei, which originates from the existence of intrinsic angular momentum (spin). The presence of a magnetic field B removes the degeneracy of the nuclear spin orientational states, due to the Zeeman Hamiltonian.

$$\hat{H}_z = -\gamma\hbar\, I \cdot B \tag{2}$$

where h = $2\pi\hbar$ stands for Planck's constant, and γ for the gyromagnetic ratio. In NMR spectroscopy the direction of the static external field B_0 is defined as the z-direction, so we have.

$$\hat{H}_z = -\gamma\hbar\hat{I}_z\hat{B}_0 \tag{3}$$

The interaction causes a precessional motion of the spins with the Larmor frequency, $\nu_L = \frac{\omega_L}{2\pi}$, given by

$$\omega_L = -\gamma B_{Loc} \tag{4}$$

and we can define:

$$B_{Loc} = B_0 + B_{int} \tag{5}$$

where B_{int} are additional inner field components originating from internal interactions of the nuclei in local magnetic on local fields created by the structural and environment.

Solution of the Schrödinger equation for nuclei with spin quantum number I results in 2I+1 eigenstates with energies.

$$E_{mI} = \hbar\omega_L m_I \tag{6}$$

defined by the value of the orientational quantum numbers *m* and *I*.

Transitions between adjacent states (m→m+1 and m→ m-1) are allowed, provided the resonance condition is fulfilled:

$$\Delta E = \hbar\omega_L \tag{7}$$

Figure 2.5 illustrates the situation for the case of a spin 5/2 nucleus.

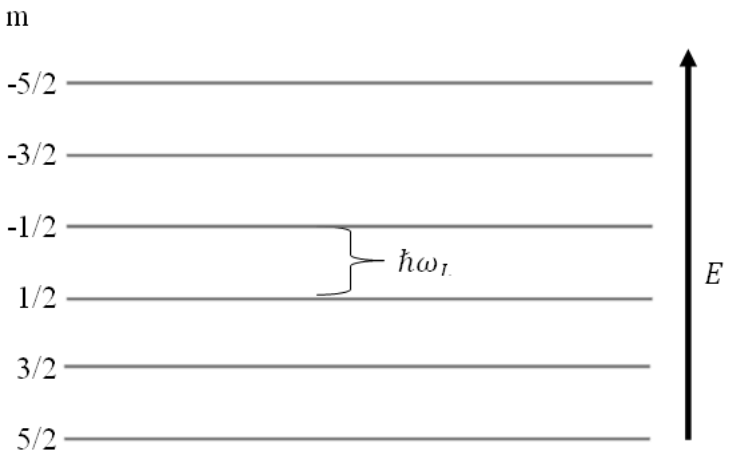

Figure 2.5 - Energy levels from the Zeeman interaction for a spin 5/2 nucleus.
Source: By the author

If the internal interaction energies are significantly smaller than the Zeeman energies, their influence on the spectra can be calculated from perturbation theory, and the total Hamiltonian can be represented by equation (7)

$$\hat{H} = \hat{H}_z + \hat{H}_{MS} + \hat{H}_D + \hat{H}_Q \quad (8)$$

where $\hat{H}_{MS}$ stands for the magnetic shielding, $\hat{H}_D$ for the dipole-dipole interaction, and $\hat{H}_Q$ for the nuclear electric quadrupole interactions, which occur for nuclear spins with I > ½.

2.2.1 MAGNETIC SHIELDING

The applied external magnetic field is the origin of induced currents in the electron shells resulting in additional magnetic field components contributing to the effective magnetic field experienced by the nuclei and determining their effective precession frequencies. These magnetic fields may be oriented either along or opposed to the external field direction, depending on if it is from a diamagnetic or paramagnetic property. The interaction originated by the secondary field produced by the electrons with the nucleus is called the shielding interaction, and it contributes to the effective magnetic field experienced by the nucleus.

In general, magnetic shielding (MS) is an anisotropic quantity. Because of this anisotropy, the MS depends on the orientation of the molecules with respect to the external field. This anisotropy has its most important consequences for powder samples,

producing inhomogeneous broadening of the resonance line. The MS is traditionally represented as a rank 2 tensor given by

$$\overleftrightarrow{\sigma} = \begin{pmatrix} \sigma_{XX} & \sigma_{XY} & \sigma_{XZ} \\ \sigma_{YX} & \sigma_{YY} & \sigma_{YZ} \\ \sigma_{ZX} & \sigma_{ZY} & \sigma_{ZZ} \end{pmatrix} \tag{9}$$

This tensor can be diagonalized by transformation into the Principal Axis System (PAS), with elements σ_{ii}^{PAS} $(i = x, y, z)$ reported following the convention.

$$|\sigma_{yy}^{PAS} - \sigma_{iso}^{PAS}| \leq |\sigma_{xx}^{PAS} - \sigma_{iso}^{PAS}| \leq |\sigma_{zz}^{PAS} - \sigma_{iso}^{PAS}| \tag{10}$$

The MS modifies the Zeeman interaction according to

$$\hat{H}_{MS} = \gamma I \overleftrightarrow{\sigma} B_0 \tag{11}$$

It is useful to describe the isotropic (σ_{iso}), anisotropic ($\Delta\sigma$) and asymmetric components (η) from the linear combination of the principal axis components, according to

$$\begin{aligned} \sigma_{iso} &= 1/3\left(\sigma_{xx}^{PAS} + \sigma_{yy}^{PAS} + \sigma_{zz}^{PAS}\right) \\ \Delta\sigma &= \sigma_{zz}^{PAS} - \frac{1}{2}\left(\sigma_{xx}^{PAS} + \sigma_{yy}^{PAS}\right) \\ \eta &= \frac{\sigma_{xx}^{PAS} - \sigma_{yy}^{PAS}}{\sigma_{zz} - \sigma_{iso}} \end{aligned} \tag{12}$$

From the definitions above, it is possible to write the nuclear precession frequency (ω_L) for any orientation θ and ϕ in the PAS as

$$\omega_L = -\omega_0 \left\{1 - \sigma_{iso} + \frac{1}{2}\Delta\sigma[(3\cos^2\theta - 1) + \eta \sin^2\theta \cos 2\phi]\right\} \tag{13}$$

where ω_0 is the nuclear Larmor frequency in the absence of shielding effects (bare nucleus) and θ and ϕ are the polar and azimuthal angles of the PAS in the laboratory frame defined by the Zeeman interaction. As absolute shielding values are experimentally inaccessible (the reference state of a bare nucleus is non-existent) the frequencies of the sample under investigation are referenced to those of standard substances. In this fashion a chemical shift can be defined according to

$$\delta_{CS} = \frac{\omega_L - \omega_{ref}}{\omega_{ref}} \tag{14}$$

2.2.2 DIPOLE-DIPOLE INTERACTION

For every nuclear spin there is a magnetic moment, and these interact through space, which is called the dipole-dipole interaction. Distinct from the scalar coupling, where the nuclei use electronic polarization effects to communicate with each other, the dipolar coupling energy can be expressed by considering the through-space interaction between two point-magnetic dipoles μ_1 and μ_2 separated by a distance r as follows:

$$U = \left\{ \frac{\mu_1 \cdot \mu_2}{r^3} - \frac{3\left((\mu_1 \cdot r)(\mu_2 \cdot r)\right)}{r^5} \right\} \frac{\mu_0}{4\pi} \tag{15}$$

where U stands for potential energy and r stands for the distance vector between point-magnetic dipoles.

It is possible to substitute the classical treatment by the quantum mechanical one using the operator $\hat{\boldsymbol{\mu}}$, which is given by:

$$\hat{\mu}_{I,S} = \gamma \hbar \hat{I} \ , \gamma \hbar \hat{S} \tag{16}$$

for generic spins I and S, and then transform it to the polar coordinate system, and expand the magnetic moments in terms of the individual spin coordinates to lead to (in angular frequency units)

$$\hat{H}_D = d[\,\hat{A} + \hat{B} + \hat{C} + \hat{D} + \hat{E} + \hat{F}] \tag{17}$$

where

$$\begin{aligned}
d &= \frac{\mu_0}{4\pi} \frac{(\gamma_1 \gamma_2 \hbar)}{r^3} \\
\hat{A} &= (3\cos^2(\theta) - 1)\hat{I}_z \hat{S}_z \\
\hat{B} &= -\frac{1}{4}\left[\hat{I}_+ \hat{S}_- + \hat{I}_- \hat{S}_+\right](3\cos^2(\theta) - 1) \\
\hat{C} &= \frac{3}{2}\left[\hat{I}_z \hat{S}_+ + \hat{I}_+ \hat{S}_z\right]\sin(\theta)\cos(\theta)\, e^{-i\phi} \\
\hat{D} &= \frac{3}{2}\left[\hat{I}_z \hat{S}_- + \hat{I}_- \hat{S}_z\right]\sin(\theta)\cos(\theta)\, e^{+i\phi} \\
\hat{E} &= \frac{3}{4}\left[\hat{I}_+ \hat{S}_+\right]\sin^2(\theta)\, e^{-2i\phi} \\
\hat{F} &= \frac{3}{4}\left[\hat{I}_- \hat{S}_-\right]\sin^2(\theta)\, e^{+2i\phi}
\end{aligned} \tag{18}$$

The operators $\hat{I}_{\pm}$ and $\hat{S}_{\pm}$ are the raising and lowering operators, and θ and ϕ are the polar and azimuthal angles between the external magnetic field and the internuclear vector r as can be seen in the Figure 2.6

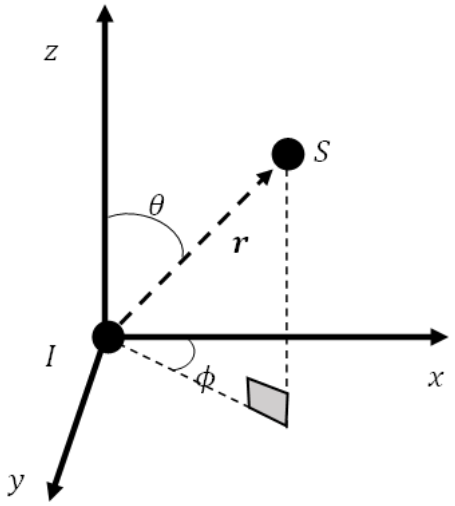

Figure 2.6 – Definition of the polar angles
Source: By the author

It is also possible to express this dipolar Hamiltonian in the tensorial form, using the dipolar-coupling tensor $\overleftrightarrow{\boldsymbol{D}}$, with principal values of -d/2, -d/2 and +d, where d stands for the dipolar coupling constant given by

$$\mathrm{d} = \hbar\left(\frac{\mu_0}{4\pi}\right)\frac{1}{\mathrm{r}^3}\gamma_1\gamma_2 \tag{19}$$

We rewrite the Hamiltonian as follows.

$$\hat{\mathrm{H}}_{\mathrm{D}} = -2\hat{\mathrm{I}}\cdot\overleftrightarrow{\mathrm{D}}\cdot\hat{\mathrm{S}} \tag{20}$$

While the dipolar coupling tensor describes how the field due to the S spin varies with the orientation of the I-S intermolecular vector under the applied field influence, the angular momenta of I and S determine the local magnetic field each of them creates.

Because the dipolar coupling tensor is traceless, there is no isotropic component, and it is always axially symmetric in its PAS, the principal axis being oriented along the I-S vector.

It is possible to consider two different cases for the dipolar coupling. One in which the I and S spins are from the same species, called homonuclear coupling, and one where they are from different species, called heteronuclear coupling.

In either case, homonuclear and heteronuclear, usually the first order perturbation theory is sufficient for calculating the effect of the dipolar interaction upon the nuclear energy levels. Considering the interaction of a spin I with its environment, we know that only certain terms, with the form $-\gamma\hbar\left(\hat{I}_x B_x^{eff}(t) + \hat{I}_y B_y^{eff}(t) + \hat{I}_z B_z^{eff}(t)\right)$ are likely to have an effect on the spin system at equilibrium significantly. Here B_z^eff denotes a static field parallel to the external field, and $B_x^{eff}(t)$ and $B_y^{eff}(t)$ denote the fields orthogonal to the applied field. The first term affects the energy splitting between the nuclear spin levels, while the last ones have a significant effect on the spin system only if they oscillate at a frequency sufficiently close to the resonance frequency.

Under the above condition, the homonuclear interaction can be described by the terms $\hat{A}$ and $\hat{B}$ resulting in a truncated Hamiltonian, or 'Secular Hamiltonian', do not modify the Zeeman energies. This also corresponds to the limit of first order perturbation theory. B is also called the "flip-flop" term, and such coupled transitions are possible only for the case where the spins I and S have identical or very similar precession frequencies to each other, which only happens in the homonuclear case. The truncated Secular Hamiltonian has the $\widehat{\mathrm{A}}$ term exclusively in case of a heteronuclear interaction.

Then we can determine both Hamiltonians as follows:

$$\widehat{H}_{\mathrm{D}}^{\mathrm{homo}} = -\frac{1}{2}\mathrm{d}(3\cos^2\theta - 1)\left[3\hat{I}_{\mathrm{Z,i}}\hat{I}_{\mathrm{Z,j}} - \mathrm{I^iI^j}\right] \tag{21}$$

$$\widehat{H}_{\mathrm{D}}^{\mathrm{hetero}} = \mathrm{d}(3\cos^2(\theta) - 1)\hat{I}_{\mathrm{Z}}\,\hat{S}_{\mathrm{Z}} \tag{22}$$

For a simple scenario of spin 1/2 for both I and S, the transition frequencies are described by.

$$\omega_{\mathrm{d}}^{\mathrm{I}}(0) = \omega_0^{\mathrm{I}} \pm \frac{1}{2}\mathrm{d}(3\cos^2\theta - 1) \tag{23}$$

where ω stands for the transition frequency in the absence of the dipolar coupling between I and S. In a polycrystalline sample containing such a two-spin system, a sum of two powder patterns is observed that resemble the one for the case of axial chemical shift

anisotropy[1][0] ("Pake pattern"). The two components correspond to the two allowed $|\Delta m_I| = 1$ Zeeman transitions, one presenting the mirror image of the other. The general form of the lineshape for both, homonuclear and heteronuclear dipolar interaction, can be seen in the Figure 2.7 - Lineshape patterns obtained in two and multi-spin 1/2 systems. . Figure 2.7 - Lineshape patterns obtained in two and multi-spin 1/2 systems. also presents the lineshape of a multispin systems, which can be considered a collection of various two-spin systems with different dipolar coupling constants. In this case the superposition of the various individual Pake patterns results in a structureless lineshape that can be approximated by a Gaussian.

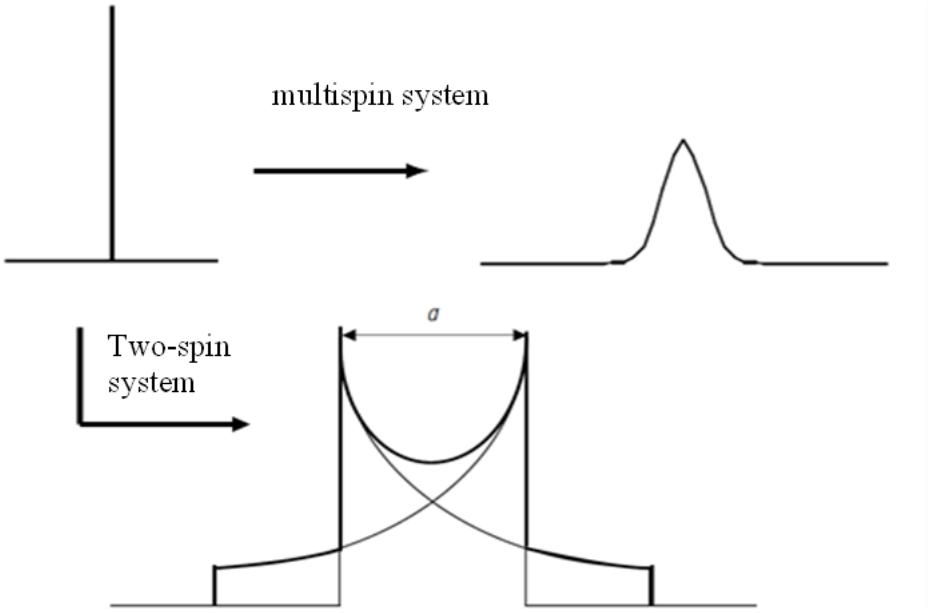

Figure 2.7 - Lineshape patterns obtained in two and multi-spin 1/2 systems.
Source: DUER. (28)

2.2.3 QUADRUPOLE INTERACTION

Among the NMR active nuclei, nearly 3/4 of them feature a spin quantum number greater than 1/2, which also implies that their charge distribution is non-spherical. These nuclei are called quadrupolar nuclei. Their electric quadrupole moments can interact with any electric field gradient present at the nucleus. The electric field gradient is naturally found in all those solids with sites non-cubic in symmetry and is produced by the electronic distribution in the vicinity of the nuclei considered.

The electric quadrupole moment arises from a non-symmetrical distribution of charge, which is represented in the scheme found in Figure 2.8 below.

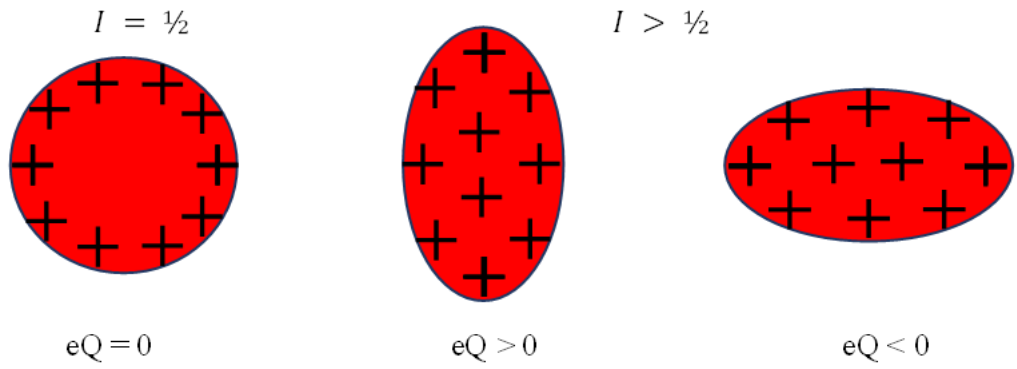

Figure 2.8 - Schematic illustration of the charge distribution in nuclei with quadrupole moment equal to, higher than, and lower than zero.
Source: By the author

This distribution causes phenomena that cannot be explained just by viewing the nuclei as point charges. It must be properly described by expanding the charge distribution function as a series of multipoles.

We may describe the interaction between the nuclear electric quadrupole moment and the electric field gradient V (a second rank cartesian tensor), in the angular frequency units, as follows.

$$\hat{H}_Q = \frac{eQ}{2I(2I-1)} \hbar \, \hat{\mathrm{I}} \cdot V \cdot \hat{\mathrm{I}} \tag{24}$$

In equation (24), Q is the quadrupole tensor, and e is the elementary charge. It is convention to define eQ as the mathematical expression for the electric quadrupole moment. Also, in equation (24), $\hat{\mathrm{I}}$ stands for the nuclear spin vector. It is convenient to define:

$$eq = V_{zz}$$

$$\eta_Q = \frac{(V_{xx} - V_{yy})}{V_{zz}} \tag{25}$$

where η_Q is the electric field gradient asymmetry parameter, and q alone has no physical meaning in SI units, but eq is the maximum component of electric field gradient tensor in the PAS.

The electric field gradient is a traceless tensor, i.e., it has no isotropic component. In the PAS, which is the frame where the electric field gradient tensor is diagonal, it is possible to rewrite the quadrupole Hamiltonian from its tensorial form equation (24) introducing the definitions of equation (25) as follows:

$$H_Q = \frac{e^2qQ}{4I(2I-1)\hbar}\left[3\hat{I}_Z^2 - I(I+1) + \frac{1}{2}\eta_Q\left(\hat{I}_+^2 + \hat{I}_-^2\right)\right] \tag{26}$$

The raising and lowering operators are given by $\hat{I}_\pm = \hat{I}_x \pm i\hat{I}_y$. We can also define from this quadrupole Hamiltonian the quadrupolar coupling constant, C_q by

$$C_q = \frac{e^2qQ}{h} \tag{27}$$

We find different definitions in literature for the quadrupole frequency, ω_Q or ν_Q. In the present work, we will use the definition found in Abragam, (15) which is a well-established definition for half integer spin nuclei in the field of nuclear quadrupole resonance (NQR), and is given by.

$$\omega_Q = \frac{3e^2qQ}{2I(2I-1)\hbar} \tag{28}$$

It is possible to change equation (26) to the laboratory frame, making it more useful for dealing with NMR experiments. Using rotation matrix to transform the coordinates from PAF into the laboratory ones, we rewrite (26) as follows:

$$\begin{aligned}\widehat{H}_Q = \frac{e^2qQ}{4I(2I-1)}\hbar\{&\frac{1}{2}(3cos^2\theta-1)\left(3\hat{I}_Z^2-\hat{I}^2\right)\\&+\frac{3}{2}\,sin\theta cos\theta\left[\hat{I}_z\left(\hat{I}_+ + \hat{I}_-\right)\right.\\&\left.+\left(\hat{I}_+ + \hat{I}_-\right)\hat{I}_z\right]\frac{3}{4}sin^2\theta\left(\hat{I}_+^2+\hat{I}_-^2\right)\}\\&+\frac{\eta_Q(e^2\,qQ)}{4I(2I-1)\hbar}\{\frac{1}{2}cos\,(2\phi\left[(1-cos^2\theta)\left(3\hat{I}_z^2\right.\right.\\&\left.-\hat{I}^2\right)+(cos^2\theta+1)\left(\hat{I}_+^2+\hat{I}_-^2\right)\left.\right]\\&+\frac{1}{2}sin\theta\left[(cos\theta cos2\theta-isin2\phi)\left(\hat{I}_+\hat{I}_z+\hat{I}_z\hat{I}_+\right)\right.\\&+(cos\theta cos2\theta+isin2\phi)\left(\hat{I}_-\hat{I}_z+\hat{I}_z\hat{I}_-\right)\\&\left.+\left(\frac{i}{4}\right)sin2\phi cos\,\theta\left(\hat{I}_+^2-\hat{I}_-^2\right)\right\}\end{aligned} \tag{29}$$

For cases where there is axial symmetry, the second term goes to zero, and (29) becomes only its first term.

Because the Zeeman interaction is the dominant term in the Hamiltonian for the spin system, then only the secular parts of H_Q affect the energies of the states of the spin system. The non-secular parts of the matrix of H_Q (in this case, the off-diagonal terms of the matrix in the Zeeman basis) are small compared with the diagonal terms provided by the Zeeman term in the total Hamiltonian. Thus, they have little effect on the eigenvalues of the diagonalized matrix of the complete Hamiltonian for the spin system $\widehat{H}_0 + \widehat{H}_Q$ (where H_0 is the Zeeman Hamiltonian). In these circumstances, the approximate energies of the spin system are found by recourse to perturbation theory. And because the splittings are less than ~1/10 of the Zeeman splitting, the second order corrections are generally enough. These corrections are given by the following:

$$\begin{aligned}E_m^{(1)} = \frac{e^2qQ}{4I(2I-1)}(I(I+1)-3m^2)\left[\frac{1}{2}(3cos^2\theta-1)\right.\\\left.-\eta cos2\phi(cos^2\theta-1)\right]\end{aligned} \tag{30}$$

$$
\begin{aligned}
E_m^{(2)} = -\left(\left[\frac{(e^2qQ)}{4I(2I-1)}\right]^2\right)\cdot\frac{m}{\omega_0} \\
&\cdot\left\{-\frac{1}{5}(I(I+1)-3m^2)(3+\eta_Q^2)\right. \\
&+\frac{1}{28}(8I(I+1)-12m^2 \\
&-3)\left[(\eta_Q^2-3)(3cos^2\theta-1)\right. \\
&\left.+6\eta_Q sin^2\theta\, cos2\phi\right] \\
&+\frac{1}{8}(18I(I+1)-34m^2 \\
&-5)\left[\frac{1}{140}(18+\eta^2)(35cos^4\theta-30cos^2\theta\right. \\
&\left.+3)+\frac{3}{7}\eta_Q sin^2\theta\,(7cos^2[\![\theta-1)\,cos\,2\phi]\!]\right. \\
&\left.\left.+\frac{1}{4}\eta_Q^2 sin^4\theta\, cos4\phi\right]\right\}
\end{aligned}
\tag{31}
$$

where m denotes the magnetic quantum number associated with the Zeeman level and $\eta = \eta_Q$ is the EFG asymmetry parameter.

Because the second order perturbation theory brings a term with dependence of the inverse of Larmor frequency, this term diminishes with increasing field strength.

Figure 2.5 can be redrawn taking in consideration corrections of first and second orders, which lead us to the distribution of the energy levels presented in Figure 2.9.

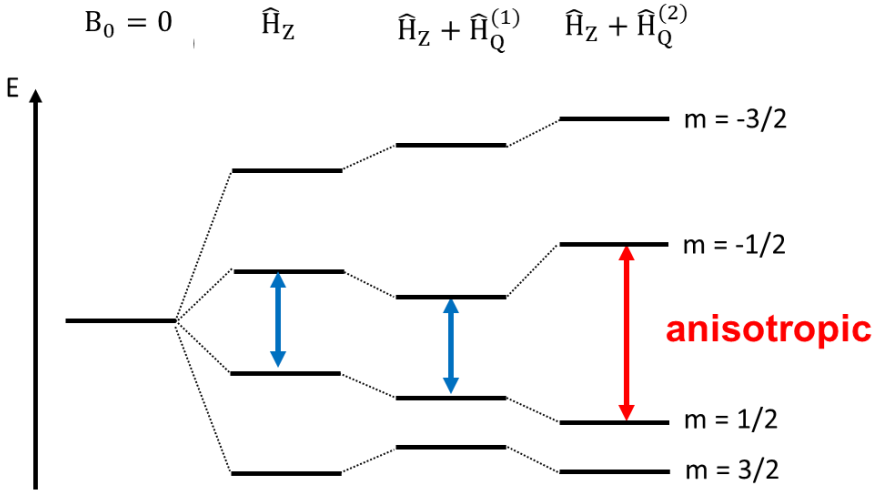

Figure 2.9 - Scheme of the splits of energy level for Zeeman hamiltonian, and first and second order correction for quadrupolar hamiltonian.
Source: By the author

The central transition remains unaltered by the quadrupolar interaction in the limit of first-order perturbation theory. However, when the quadrupolar interaction reaches a sufficient magnitude relative to the Zeeman interaction the quantum mechanical treatment

requires second order perturbation theory. In this case, there will be an anisotropy component leading to perturbations in the central transition. The visual representation, using blue arrows, depicts the central transition and the preservation of the energy gap, while the red arrows indicate the anisotropic perturbations imposed on the energy gap.

The correction made by the first and second order of the perturbation theory result in different lineshapes, as can be seen in Figure 2.10, which presents the NMR lineshape of spectra of central transitions of half-integer spin numbers for different asymmetry parameters.

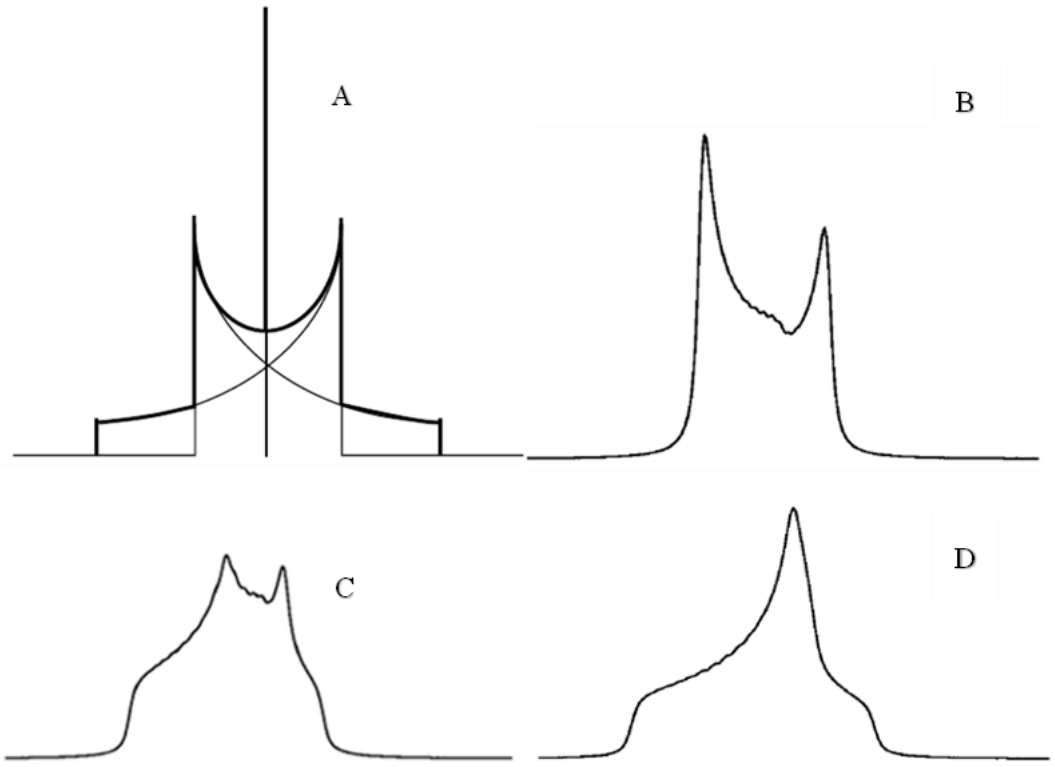

Figure 2.10 – Spectra on the central transition of half-integer spins. (A) is obtained from the first order perturbation. (B) to (D) are for the second order perturbation theory, where (B) has $\eta = 0$, (C) has $\eta = 0.5$, and (D) has $\eta = 1$.
Source: DUER. (28)

To model the lineshapes of NMR in glasses with strong quadrupolar coupling, Czjzek modelling can be a good alternative. The Czjzek distribution consists in a mathematical model that describes the probability of finding local environments with specific values of quadrupolar coupling strength (C_Q) and asymmetry (η) in a disordered system. (16 - 17) The model assumes that in the absence of disorder, the chemical environment of the nuclei is fully symmetric, meaning that the electric field gradient

(EFG) is zero. However, when disorder is introduced, the EFG components are considered to follow a normal statistical distribution. The Czjzek probability function is described by an expression that takes into account these factors, and it is commonly used to analyze and interpret the quadrupolarly perturbed NMR spectra of disordered systems such as glasses (16 - 17)

$$P(C_Q,\eta) = \frac{1}{\sqrt{2\pi\sigma^5}} C_Q^4 \eta \left(1 - \frac{\eta^2}{9}\right) exp\left[\frac{-C_Q^2\left(1+\frac{\eta^2}{3}\right)}{2\sigma^2}\right] \qquad (32)$$

where σ is the width of the distribution.

2.3 SOLID-STATE NMR SPECTROSCOPY TECHNIQUES

In the solid state most of the nuclear spin interactions are anisotropic, depending on the molecular orientation within the applied magnetic field of the NMR experiment. For this reason, any change in the molecular orientation is followed by a change in resonance frequency. As discussed below to record faithful lineshapes not affected by distortions the Hahn spin echo method can be used. (18) The signal-to-noise ratio in certain situations can be enhanced by accumulating multiple echoes, using the Carr-Purcell-Meiboom-Gill technique. (19 - 20) If the width of the anisotropically broadened lineshape exceeds that of the pulse excitation window, special wideband excitation methods can be employed, the most important one being the **W**ideband **U**niform **R**ate with **S**mooth **T**runcation (WURST) method. A brief description of these methods is given below. Beyond these techniques used for recording wideline spectra, special selective averaging techniques can be exploited to simplify the complex NMR Hamiltonian given in the previous equation. The methods relevant within the context of the present dissertation are (a) Magic Angle Spinning (MAS) for determining isotropic chemical shift and nuclear electric quadrupolar couplings and (b) the static spin echo decay method for measuring the homonuclear dipole-dipole interaction strength.

2.3.1 THE HAHN SPIN ECHO TECHNIQUE

The Hahn spin echo (HSE) is an essential technique to study nuclei which present

a transverse relaxation time (2) short or comparable to the dead time of the equipment, compromising the acquisition of the signal.

After irradiating the required radio frequency pulse, the coils in the equipment require a transient time to dampen the mechanical vibration, also referred to as ringing, which would produce artificial signals unrelated to those arising from nuclear precession. To avoid this, some delay is required from the excitation moment to the signal acquisition, and this characteristic time is the so-called deadtime.

The HSE NMR consists of two pulses in sequence as presented in Figure 2.11. In the rotating frame, the first pulse changes the net magnetization from z-axis to the positive direction of the *y*-axis by a rotation of $\pi/2$ over the *x*-axis. The spins dephase owing their differences in Larmor precessional frequencies during a time τ and then a second pulse with nutation angle π, also applied along the *x*-rotating frame axis, changes their orientation by 180°. After another interval of time τ the spins have rephased, having their maximum magnetization along the negative *y*-axis direction. Because the time from τ can be adjusted to be bigger than the equipment deadtime, and this combined to the fact $T_2 > T_2^*$, the loss of signal due HSE is far less than the loss of signal for a single pulse of $\pi/2$ technique.

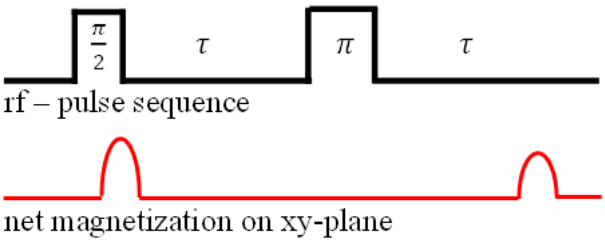

Figure 2. 11 Representation of the HSE pulse sequence using block diagram (black), and the intensity of net magnetization in the xy-plane.
Source: By the author

2.3.2 THE CARR-PURCELL-MEILBOOM-GILL SEQUENCE

The Carr-Purcell-Meilboom-Gill (CPMG) sequence (21) is a sequence generating multiple spin echoes after which each one of which the FID is recorded. The sequence starts as a traditional Hahn Echo experiment, and after the spins starts losing their coherence again, a new 180° pulse is applied and the spins rephase again.

The complete time domain series resulting from the outputs each of the *M* repeated steps strung together is then Fourier transformed. This experiment has the effect of splitting the quadrupole echo powder pattern into a manifold of spikelets separated by $\frac{1}{\tau_a}$, where τ_a stands for the acquisition time in each of the *M* echoes. The use of this technique generates a sensitivity enhancement by one order of magnitude (22) and is particularly useful when $T_2^* << T_2$ and T_1. Figure 2.12 shows the scheme of the pulse sequence. The sequence consists of a standard quadrupole echo pulse sequence, after which the echo is recorded. Following it there is a series of refocusing 180° pulses, with a complete echo being recorded after each.

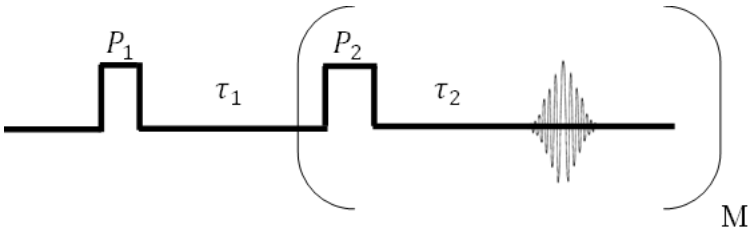

Figure 2.12 - Schematic of CPMG sequence.
Source: By the author

The echoes from the present pulse sequence can be summarized as in Figure 2.13

.

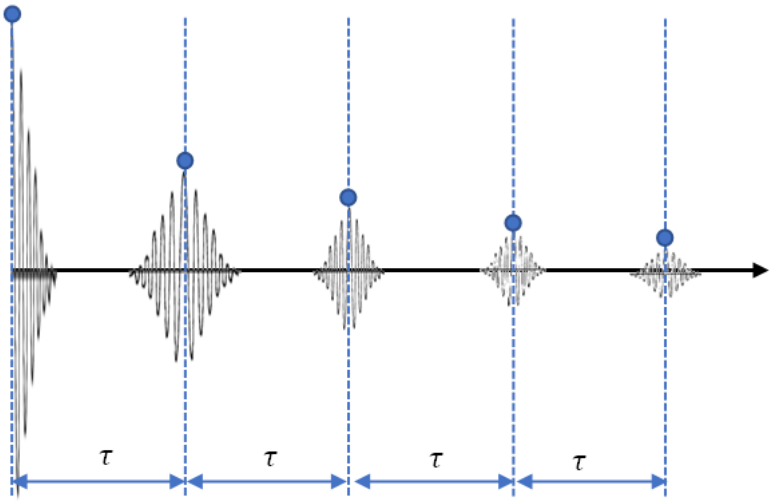

Figure 2.13 - Echoes from CPMG sequence.
Source: By the author

2.3.3 THE WIDEBAND UNIFORM RATE SMOOTH TRUNCATION (WURST) METHOD

For modern NMR spectroscopy, amplitude- and phase-modulated rf-pulses are routinely incorporated, relying on a variety of different pulse schemes which have been developed over the past 30 years. The present technique, WURST, was first introduced in 1995 by Kupče and Freeman as a means of achieving broadband adiabatic inversion of magnetization for solution-state ^{13}C decoupling at high magnetic field strengths. Over the years these pulses have found use in an increasingly diverse range of applications in solid-state NMR.

The shape of the pulse in the present varies significantly with a parameter *N* which changes the shape from a rectangular pulse to a hyperbolic secant-like pulse for the range of *N*. The acronym WURST means "sausage" in German and refers to the shape the pulse takes as this *N* parameter moves from large values to smaller values. The pulse amplitude $\omega_1(t)$ is given by the following function of time and *N*:

$$\omega_1(t) = \omega_{max}\left(1 - \left|\cos\left(\frac{\pi t}{\tau_W}\right)\right|^N\right) \tag{33}$$

where ω_{max} stand for the maximum RF amplitude and τ_w is the pulse duration.

The phase of the pulse is modulated as a quadratic function of time, as described below:

$$\phi(t) = \pm 2\pi\left\{\left(\nu_{off} + \frac{\Delta}{2}\right)t - \left(\frac{\Delta}{2\tau_w}\right)t^2\right\} \tag{34}$$

where Δ is the total sweep range and ν_{off} gives the offset frequency for the centre of the sweep, both are given in Hz, and this is known as "chirp" modulation.

In Figure 2.14 there is a representation of the pulse amplitude and phase for different parameters.

In Figure 2.14, part (a) contains WURST pulse profiles for various values of the power index *N* as shown. (b) is the phase modulation for WURST pulse of 100 μs in length and with a sweep range of 400 kHz. Here, the direction of the frequency sweep is

positive. (c) is the same as (b), but with the vertical scale restricted to the range $0 - 2\pi$. (d) is the same as (c) but with the direction of the frequency sweep reversed.

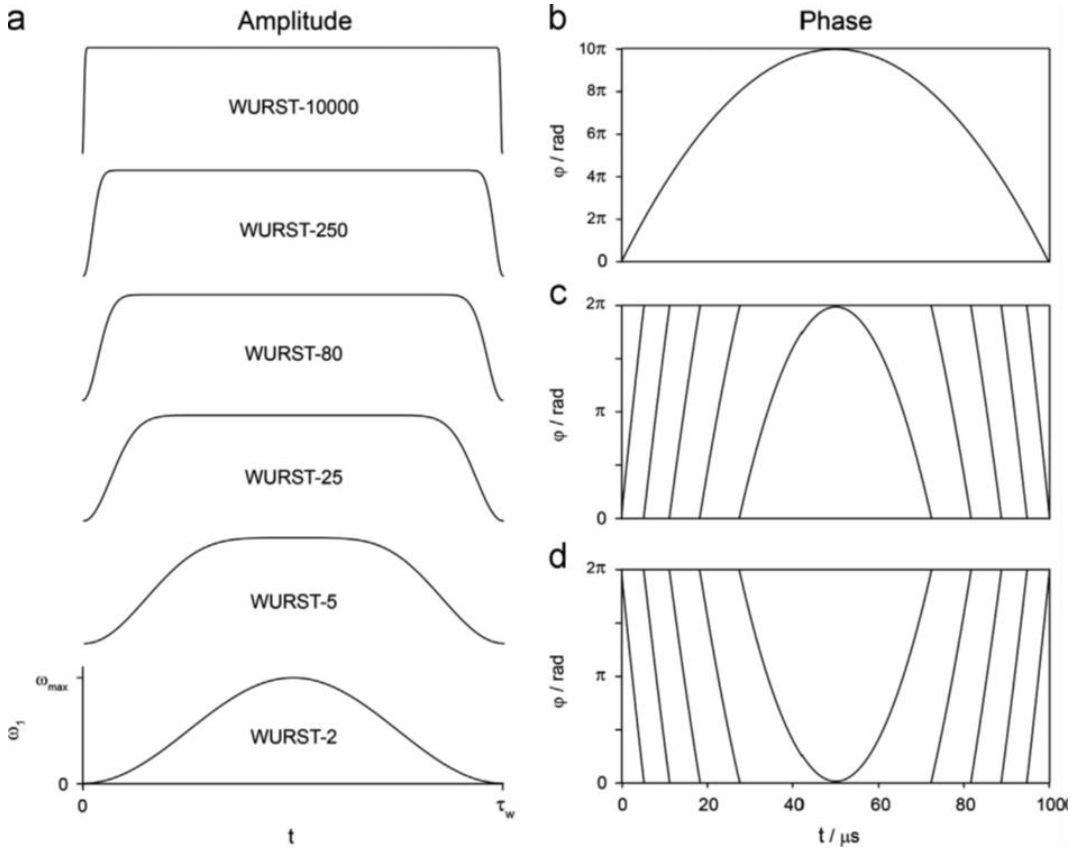

Figure 2.14 – WURST pulse profiles for various values of power index and phase modulation. Source: O'DELL. (22)

In practice, WURST pulses can be seen as a train of n standard RF pulses all applied at the RF transmitter frequency, which is fixed. The amplitude and phase of these individual pulses are determined through the equations (31) and (32) by setting the values for the parameters ω_{max}, τ_w, Δ, and ν_{off} . (23)

2.3.4 THE MAGIC ANGLE-SPINNING TECHNIQUE: SPIN-1/2 NUCLEI

Liquid-state NMR spectra rarely show the effects of inhomogeneous broadening interactions such as chemical shift anisotropy and dipolar coupling. These effects are dependent on the orientation of the shielding and dipolar tensors with respect to the external magnetic field.

Because molecules in liquid move randomly in such a way that every possible orientation in relation to B_0 is visited for a small time, the average of this term goes to zero on the NMR timescale. For the solid state, the anisotropies present in the NMR

Hamiltonian result in a wide frequency dispersion in polycrystalline and amorphous samples, arising from orientational statistics.

This effect can be removed by the technique of Magic Angle Spinning (MAS). By spinning the sample rapidly about an axis inclined by 54.74°, known as the "magic angle", (which is the root of the second Legendre polynomial) relative to the magnetic field direction, is possible to mitigate and even remove the secular anisotropic contributions of the spin interactions. (24 - 25)

For a nucleus featuring a nuclear spin quantum number of 1/2, the charge in the nucleus presents a symmetric distribution of charge which implies a zero moment, and for this reason the main broadening effects present in the NMR measurements are dipole-dipole interaction and the magnetic shielding anisotropy. Both are strongly related with to the angle of the principal axis of the molecule with the external magnetic field with $(3\cos^2(\theta) - 1)$, which goes to zero at 54.7°.

If the spinning frequency is lower than or comparable to the width of the static lineshape in frequency units, the narrowed signal at the isotropic chemical shift is accompanied by spinning sidebands (ssb), which are sharp lines set apart of the isotropic chemical shift by an integer multiple of the spinning speed of the rotor. Their intensity distribution depends on the ratio of the spinning frequency to the overall width of the static lineshape. In the slow spinning limit, the spinning sideband intensity profile measured forms the envelope of the static powder pattern. The peak observed at the isotropic chemical shift will be independent of spinning frequency. To illustrate the effect of slow speed MAS-NMR, see Figure 2.15.

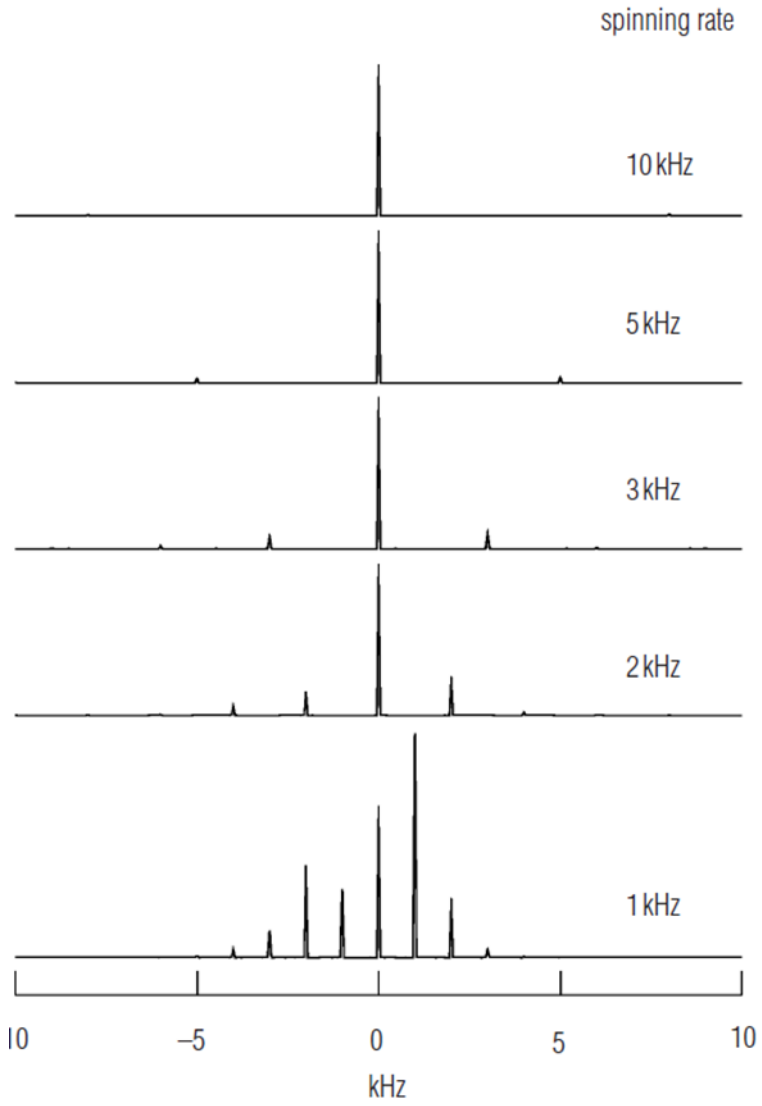

Figure 2.15 - Schematic illustration of the magic-angle spinning spectra for different spinning speeds.
Source: DUER. (28)

2.3.5 THE MAGIC-ANGLE SPINNING TECHNIQUE: QUADRUPOLAR NUCLEI

The Hamiltonian of nuclei featuring spin quantum number larger than ½ in non-cubic environments, contains the quadrupolar interaction that influences the NMR spectra. For the first order perturbation theory the quadrupolar satellites are broken up into a set of sharp spinning sidebands. However, in the case of second order quadrupolar perturbations the anisotropy effects on the static lineshape are not averaged by the MAS experiment, due to a more complex orientational dependence and, as a consequence, the MAS spectra retain residual anisotropic broadening.

The lineshapes measured for such quadrupolar nuclei under MAS conditions are still much narrower than the powder patterns observed under static conditions, and their specific shapes depend on C_Q, η_Q and δ_{iso}. In her book, Duer (26) shows the effect of magic-angle spinning (MAS) on the central transition lineshape for a half-integer quadrupolar nucleus, which follows in Figure 2.16.

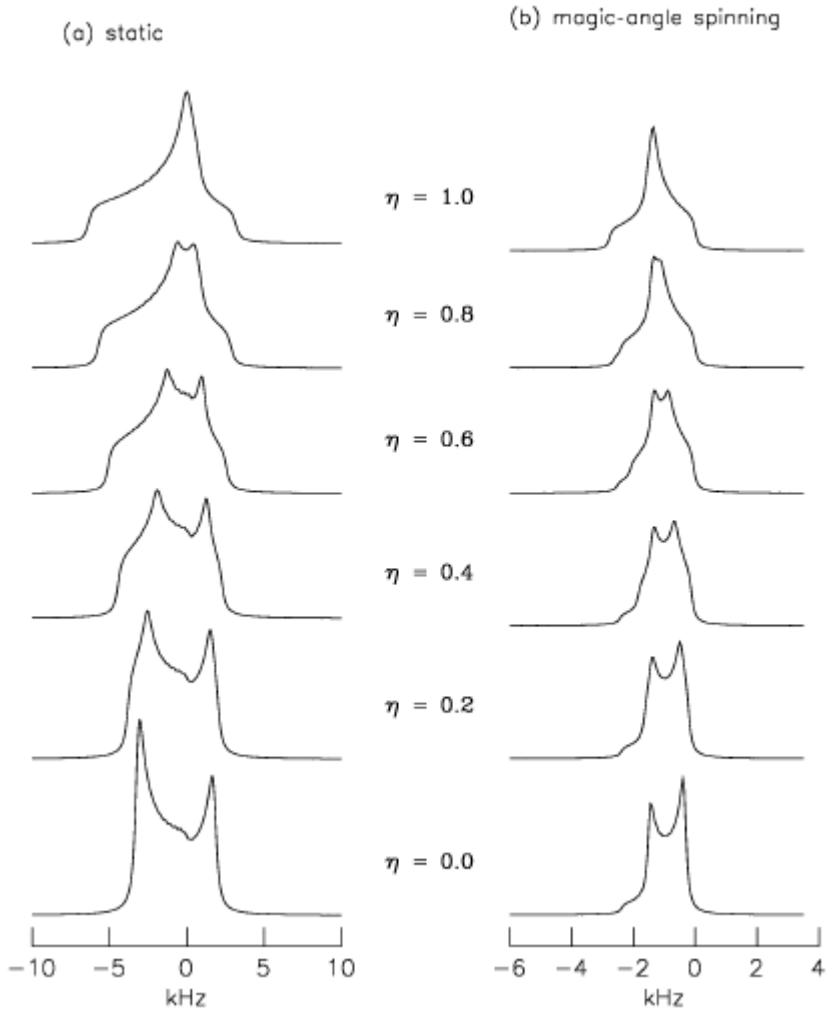

Figure 2.16 - Effect of MAS on the central transition lineshape for different values of EFG asymmetry parameters.
Source: DUER. (28)

While for spin-1/2 nuclei this central peak is located at the isotropic chemical shift whereas for quadrupolar nuclei an isotropic second order quadrupolar shift has to be taken into consideration. (27) Finally, if the spinning rate of the sample is not fast enough compared to the anisotropy of the interaction being spun out by MAS-NMR (three or four times greater), the spinning produces a set of spinning sidebands (SSB) in addition to the central peak.

2.3.6 MQMAS

The MQMAS (multiple-quantum–magic-angle spinning) technique is a two-dimensional echo experiment producing a spectrum in which one of the dimensions is not influenced by the second order quadrupolar broadening, which makes it a powerful tool to distinguish different sites in anisotropically broadened MAS-NMR spectra of quadrupolar nuclei affected by second order quadrupolar perturbations such as ^{27}Al. The technique correlates the evolution of the single-quantum coherences generated from the spin system and observed via regular single pulse excitation, with the evolution of multiple quantum coherences generated by two-pulse excitation, followed by suitable coherence selection via phase cycling and double Fourier transformation. As a result the first order quadrupolar broadening is removed, leading to isotropic signal in one dimension.

Among the techniques for studying glass structure, MQMAS, particularly the triple-quantum experiment (TQMAS), has shown to be the best technique for resolving or showing the absence of small concentrations of AlO_5 and AlO_6 groups in glasses whose ^{27}Al spectra are dominated by the signal of AlO_4 sites. (22 - 28) The pulse sequence is given in Figure 4.17.

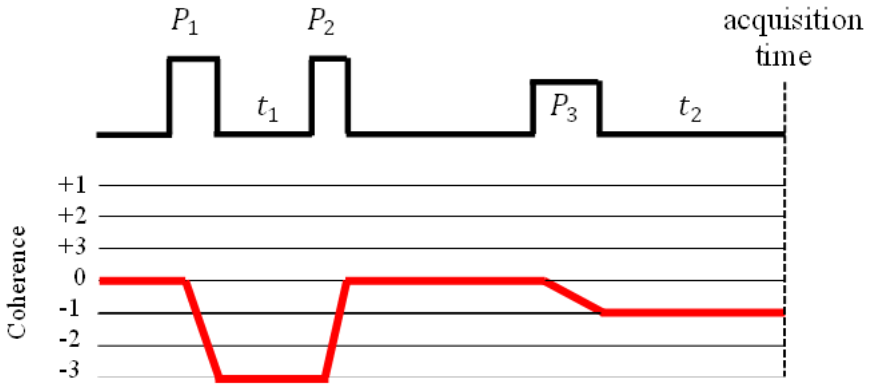

Figure 2.17 - Pulse sequence scheme and the coherence path using the z-filter.
Source: By the author

The sequence presented above consists of a three-pulse z-filter sequence, where P_1 and P_2 are hard pulses, while P_3 is a soft detection pulse. While t_1 is the time the coherence evolves, t_2 is the echo time. leading through an asymmetric coherence path that results in a large suppression of phase problem and line shape distortion. (29) The first pulse P_1 is the one responsible for exciting all the possible coherences under the MAS-Hamiltonian. Then these coherences evolve for a given time t_1, being refocused by

the second pulse P_2 to coherence 0, and a third pulse P_3 converts this zero-quantum coherence to an observable magnetization.

While the 2D-spectra recorded in the dimensions t_1 and t_2 being submitted to the Fourier transformation, still contain anisotropic contributions in both dimensions, the anisotropy can be removed by performing a shearing transformation, effecting a phase correction for all points prior to Fourier transformations along F_1. In this way a significant enhancement can be produced for the MAS-NMR spectra for nuclei whose precession frequencies are affected by second order quadrupolar effects.

From the resulting spectra, we are able to calculate the centers of gravity of the projections, and from them one can extract the parameters below (30):

$$\delta_{iso} = \frac{17}{27}\delta_{F1} + \frac{10}{27}\delta_{F2} \tag{35}$$

$$SOQE = Cq\left(1 + \frac{\eta^2}{3}\right)^{\frac{1}{2}} = \sqrt{\left\{\frac{170}{81}\frac{[4S(2S-1)]^2}{[4S(S-1)-3]}\right\}} \times \nu_0 \times 10^{-3} \tag{36}$$

3 EXPERIMENTAL

With the intent of studying the NMR spectra of ^{25}Mg in glass, we characterized five different ^{25}Mg enriched silicate and aluminosilicate samples along with some crystalline model compounds at natural abundance. The samples here studied were provided by Professor Philip Salmon, University of Bath. In the present section the samples are presented, as well as the parameters used in each technique applied in this work.

3.1 SAMPLE PREPARATION

The enstatite ($MgSiO_3$) samples were prepared as outlined in a study by (31) using either natural MgO (>99%) or isotopically enriched ^{25}MgO and SiO_2 (>99%). The isotopic enrichment of the ^{25}MgO used in sample preparation was determined to be 1.00(2) % of ^{24}Mg, 98.49(3) ^{25}Mg, and 0.51(1) % ^{26}Mg.

An isotopically enriched diopside glass ($CaMgSi_2O_6$) was fabricated by using the technique outlined by (32) with powders of ^{25}MgO (0.81% ^{24}Mg, 98.79% ^{25}Mg, 0.40% ^{26}Mg), $CaCO_3$ (>99%), and SiO_2 (>99%). The powders were heated overnight at 800 °C and then melted in air at a processing temperature of T_{proc} ~1492 °C in a Pt/10% Rh crucible. The melt was rapidly cooled by immersing the bottom of the crucible in water, and the process was repeated multiple times to ensure homogeneity. A natural isotopic abundance diopside glass was also prepared by using powders of nat MgO (Aldrich, ≥99.99%), $CaCO_3$ (Aldrich, ≥99.999%), and SiO_2 (Alfa Aesar, 99.9%). The powders were heated overnight at 800 °C and mixed by shaking. A batch of mass ~3 g was transferred to a Pt/10%Rh crucible, melted by heating from room temperature to T_{proc} = 1550 °C in about 1 h, and held at this temperature for 1 h. The melt was cooled rapidly by placing the bottom of the crucible onto a liquid-nitrogen cooled copper block. The sample was then ground, remelted in a furnace at 1550 °C for 1 h, and cooled again. The mass loss was 0.08% on the first melt and 0.15% on the second melt, which was attributed to the loss of water re-adsorbed during the preparation procedure.

The aluminosilicate samples were prepared from a combination of natural magnesium oxide, isotopically enriched ^{25}MgO, aluminum oxide and silicon dioxide. The powders were calcined at 1000 °C for 2 hours in a Pt or Pt/10%Rh crucible. The aluminosilicate samples were designated by MAS x (x = 226, 25, or 37.5) and were made by mixing the

appropriate mass of each powder, then transferring the mixture to a Pt/10%Rh crucible and drying at 1000 °C for 10 minutes to remove water adsorbed during the weighing and mixing process. The mixture was then melted by heating to a processing temperature of either 1550 °C or 1650 °C and held at this temperature for 1 hour. The melt was then quenched by placing the bottom of the crucible onto a liquid nitrogen cooled copper block. The mass loss on melting was less than 0.3%, which was attributed to the loss of re-adsorbed water. The MAS 226 glasses were made by adding silicon dioxide to MAS 25 after it had been finely ground and dried at 200 °C for 1 hour. The powders were mixed by shaking and melted in a Pt/10%Rh crucible at 1650 °C for 1 hour before being quenched.

Table 1 - The processing temperature T_{proc} and mol percentage of the diopside, enstatite, and magnesium alumino silicate glasses.

SAMPLE	SiO_2 (%)	MgO (%)	CaO (%)	Al_2O_3 (%)	T_{proc} (°C)
Diopside (CMS 25)	60	25	25	0	1492-1550
Enstatite ($MgSiO_3$)	50	50	0	0	1650
MAS 37.5	50	37.5	0	12.5	1550
MAS 25	50	25.0	0	25.0	1550
MAS 226	60	20.0	0	20.0	1550

Source: By the author

Before the repetition of the melting and quench process, each sample was ground. The loss of mass during the first melt was ≤0.46% and ≤0.29% during the second melt, which can be attributed to the loss of re-adsorbed water. The stoichiometry of enstatite glasses was determined using electron microprobe analysis, and their density was calculated using Archimedes' principle with toluene as the immersion medium (31) The stoichiometry of the other glasses was obtained from the batch composition, and their density was determined by He pycnometry Table 1.

To differentiate natural and isotopic enriched samples, we use the prefix iso for the enriched ones while nat stands for the ones with natural abundance of ^{25}Mg. The studied samples were:

- iso MgSiO3 (Enstatite)
- iso CMS 25 (Diopside)
- nat / iso MAS 25
- nat / iso MAS 226
- nat / iso MAS 37.5

3.2 SOLID STATE NMR

3.2.1 ^{29}SI AND ^{27}AL NMR

The NMR spectra of ^{29}Si nuclei were obtained at room temperature using a magnetic field strength of 5.64 T on an Agilent DD2 spectrometer with specialized MAS-NMR probes spinning at a rate of 5 kHz, with 90-degree pulses of 4 μs duration and a relaxation delay of 900 s. (33)

NMR spectroscopy on ^{27}Al nuclei was performed at room temperature at a magnetic field strength of 14.1 T using a Bruker Avance Neo 600 spectrometer that was outfitted with specialized NMR probes. Rotors of 2.5 mm were employed, spinning at rate of 25 kHz, with 90° pulses of 1.2 μs length and a relaxation delay of 0.5 seconds. TQMAS-NMR (Triple-Quantum Magic Angle Spinning) experiments on ^{27}Al nuclei employed a standard three-pulse zero-filtering sequence, with pulse lengths of 3.9 and 1.7 μs for the generation and re-conversion of triple-quantum coherences, respectively, at a power level of 120 W. A soft detection pulse of length 10.2 μs and power level 1.5 W was used for the zero-to-single quantum conversion, and the relaxation delay was 0.1 seconds. The series of free induction decay (FID) signals obtained from the TQMAS measurements were Fourier transformed and sheared using the software TopSpin to obtain the separate isotropic (F_1) and anisotropic (F_2) dimensions. The isotropic chemical shift δ_{iso} and quadrupolar product P_Q were derived from the sheared two-dimensional spectra using the expressions (37) and (38)

$$\delta_{iso} = \frac{17}{27}\delta_{F1} + \frac{10}{27}\delta_{F2} \tag{37}$$

$$P_Q = C_Q\left(1 + \frac{\eta^2}{3}\right)^{\frac{1}{2}}$$

$$= \sqrt{\frac{170}{81}\frac{[4S(2S-1)]^2}{[4S(S+1)-3]}(\delta_{F1} - \delta_{F2})} \cdot \nu\_0 \cdot 10^{-3} \tag{38}$$

The chemical shifts in the F_1 and F_2 dimensions, denoted as δF_1 and δF_2, were obtained by integrating over the displaying spectral intensity. The parameters C_Q and η ($0 \leq \eta \leq 1$) describe the magnitude and symmetry of the electric field gradient tensor

interacting with the nuclear electric quadrupole moment, respectively. The Zeeman frequency is represented by υ_0, and *S* represents the spin quantum number of the nucleus.

The MAS NMR spectra were modelled using the DMfit program (34). Gaussian/Lorentzian line shapes were assumed for (i) the spin 1/2 ^{29}Si nucleus and (ii) the spinning sidebands related to the $|m| = 1/2 \leftrightarrow |m| = 3/2$ satellite transitions for the ^{27}Al nucleus. The second-order quadrupolar broadening effects are insignificant for these transitions in the case of spin-5/2 nuclei. (35). The line shapes of the ^{27}Al central transition were simulated using the Czjzek model, (17) discussed above.

The chemical shifts of ^{29}Si and ^{27}Al were reported in relation to tetramethyl silane (TMS) and 1M $Al(NO_3)_3$ aqueous solution, respectively. Solid kaolinite ($\delta_{iso}(^{29}Si)$ = 91.5 ppm) and AlF3 (δiso(27Al) = −16 ppm) were used as secondary references for 29Si and 27Al, respectively.

3.2.2 ^{25}MG MAS AND STATIC NMR

Room temperature ^{25}Mg MAS NMR spectra were obtained at 36.8 MHz with the use of a 14.1 T magnetic field, through the rotor-synchronized Hahn spin echo method, on a Bruker Avance Neo 600 spectrometer. The samples were placed in 3.2 mm rotors and spun at 20.0 kHz. To ensure non-selective nutation frequencies of 25 MHz, as measured on cubic MgO, the power level was adjusted accordingly. The pulse lengths were optimized by maximizing the echo intensity in a t_p-τ-2t_p-τ sequence, where τ was set to 50 μs and t_p to 9 μs and 25 W power. The relaxation delay was 0.5 seconds.

The static ^{25}Mg NMR spectra were measured using a Wideband Uniform Rate Smooth Truncation (WURST) pulse sequence (23) combined with the Carr–Purcell–Meiboom–Gill (CPMG) echo train acquisition scheme (19 - 20). The signal was acquired at multiple different base frequencies, corresponding to resonance offsets from the center of the *m* = 1/2 to *m* = -1/2 transition. These spectra were taken to test for the presence of noncentral satellite transitions, which are affected differently by the anisotropy of nuclear electric quadrupolar interactions. The WURST experiments were done using excitation and refocusing pulses with a length of 50.0 μs, an excitation bandwidth of 1 MHz, and a recycle delay of 0.2 s. The pulse spacing was set to give a spikelet separation of 6.7 kHz upon Fourier transformation, and the number of Meiboom-Gill loops was set to 256, and power index equals to 80.

The simulations of the ^{25}Mg MAS line shape used the Czjzek model and were performed using the ssNake (36) software. The simulations of the ^{25}Mg static line shapes also used the Czjzek model and were performed using in-house Matlab® code with SIMPSON (37) as the kernel. Details of the simulation procedures are described elsewhere. (33)

The ^{25}Mg chemical shifts are reported relative to aqueous $MgCl_2$ solution using solid nat MgO ($\delta_{iso}(^{25}Mg)$ = 27 ppm) as a secondary reference.

4 RESULTS AND DISCUSSION

4.1 ^{29}SI MAGIC ANGLE SPINNING (MAS)

Figure 4.1 shows the ^{29}Si MAS NMR spectrum of diopside enriched with ^{25}Mg. Because of the small amount of material available, the signal-to-noise ratio was severely limited. The situation is further aggravated by extremely long spin-lattice relaxation times. The presented spectra typically take around 48h to accumulate.

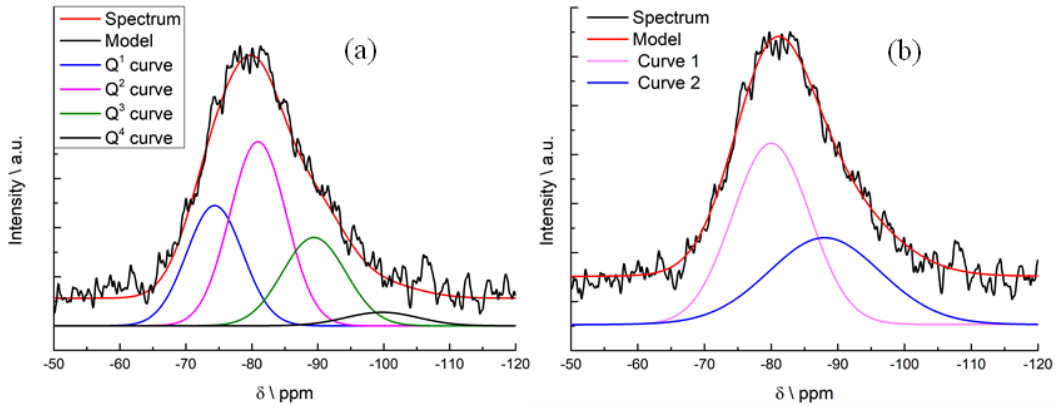

Figure 4.1- ^{29}Si MAS-NMR spectra at 5.64 T for the ^{25}Mg-enriched CMS 25 sample (a) The spectra were deconvoluted using the proposed Q^n distribution from the literature, giving a barycentre of -84 ppm. (b) Simplified two-component deconvolution, giving a barycenter of -83 ppm.

Source: By the author

Because of these limitations reliable signal deconvolution in terms of the contributions from the separate Q^n species, where *n* denotes the number of bridging oxygen atoms per SiO_4 tetrahedron, could not be obtained. The spectra are, however, consistent with previously published data (32, 38 – 42), where the simulations generally assume a distribution of Q^1, Q^2, Q^3, and Q^4 environments. (39, 41 - 42)

Differently from the literature, it is possible to see from Figure 4.1(b) that a simplification in the present spectrum can be done by using two curves, where their resultant has a strong similarity to the modelled by the four species proposed. In such analysis without pretense of individual accuracy for the individual curves, this simple modelling could be a good approximation for estimating the barycentre of the spectra of aluminum silicate glasses, particularly in spectra with poor signal-to-noise ratios.

The spectrum found for iso CMS 25 agrees with the Q^n species distribution proposal made previously. (42) With the intent of comparing Schneider's fitting approach with the two-component fitting, it was used the assumed Gaussian distributions of isotropic

chemical shifts δ_{iso} for each type of Qn unit in the graph (a), using all the experimental fitting parameters as in reference. (42)

The position and percentage of each curve fitted using Schneider's parameters, the value found by the Schneider is present in reference (42) can be found in Table 2, as well as the resultant from the deconvolution of the spectrum of iso MAS 25 for the distribution of Q^n.

Table 2 – Deconvolution parameters for the ^{29}Si MAS-NMR spectrum of sample iso CMS 25 and comparison with the values obtained in the Literature *(42)*.

Q^n	δ_{iso}\ ppm	Hugo's \ %	Schneider's \ %
Q^1	-77.5	33	28 (8)
Q^2	-84	43	43 (10)
Q^3	-92.5	20	25 (6)
Q^4	-103	4	4(1)

Source: By the author

The quantity found for each species of Q^n species follow accordingly the values from reference (42), as expected. Furthermore, results found calculating the barycenter for iso MAS 25 using only two curves with free position was consistent with this information, which validates the use of this method for the other samples.

Figure 4.2 shows the ^{29}Si MAS NMR spectra of samples with and without ^{25}Mg enrichment. All the spectra reveal certain asymmetries in the lineshape, which indicates that a single Gaussian curve may not be able to fit it properly. Figure 4.2 also shows the above-decribed attempt to fit all the data to a set of two lineshape components, without attributing a structural significance to these two components. Based on these deconvolutions it was possible to determine average isotropic chemical shifts $<\delta_{iso}>$, determined from the barycenter and the full widths at half maximum (FWHM), based on the simulated (composite) spectra. The linewidths are dominated by a distribution of isotropic chemical shifts, which arise from local variations in Si-O bond lengths and (in particular) Si-O-Si bond angles affecting different silicon atoms in the amorphous networks.

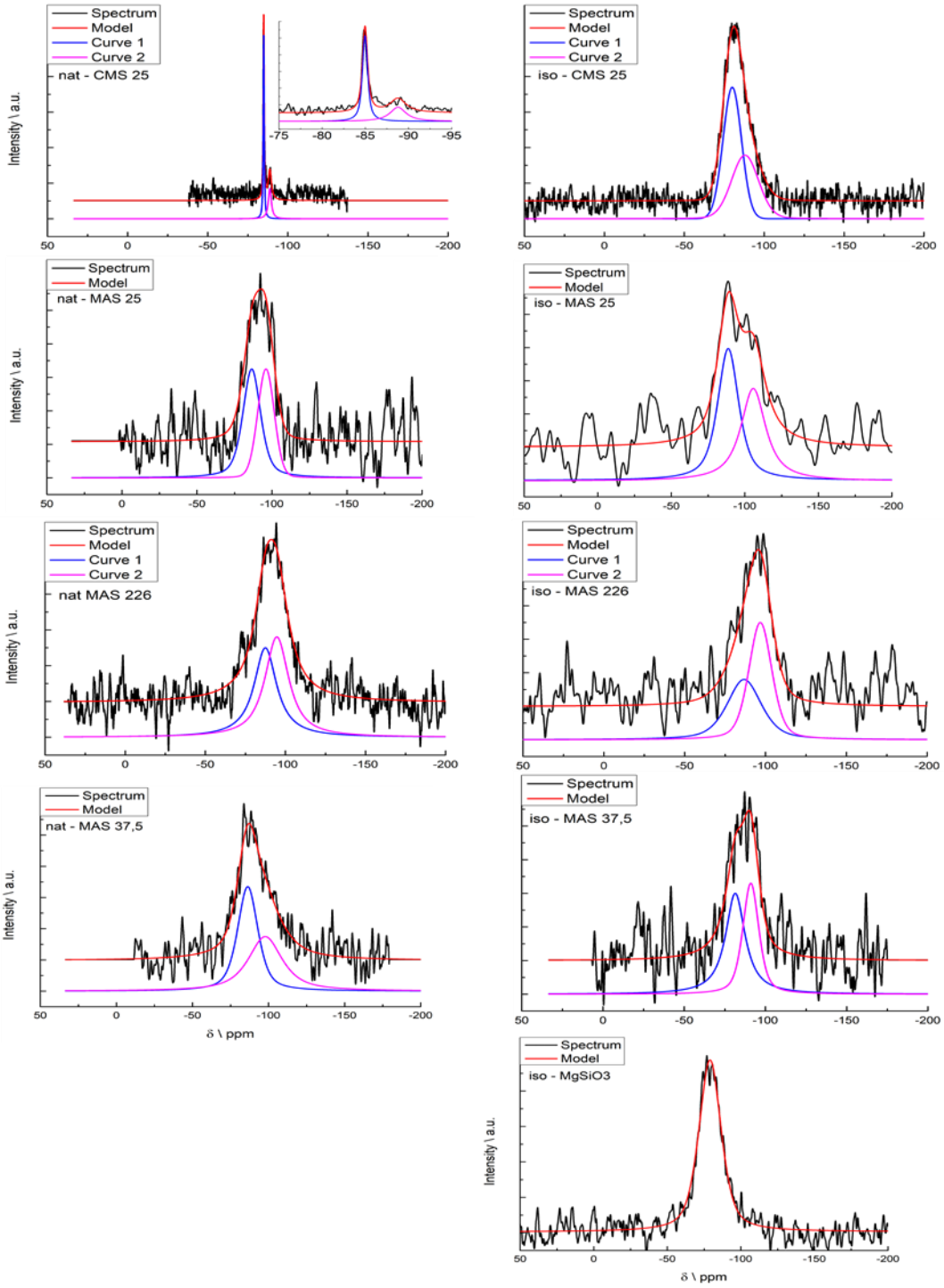

Figure 4.2 - ^{29}Si MAS-NMR spectra at 5.64 T for ^{25}Mg enriched and natural abundance samples. For those spectra that were found to have two components, the spectrum and the model were translated vertically to ease the visualization of the individual components.
Source: By the author

In principle it is expected that for glasses with the same basic composition $\langle\delta_{iso}\rangle$ and FWHM would come out identical for the samples with and without ^{25}Mg isotopic enrichment. As indicated in this is indeed found for the glass MAS 226, whereas there are stronger deviations for the other two magnesium aluminosilicate glass compositions.

The deviations are attributed to the relatively large experimental error caused by the low signal-to-noise ratio.

In the case of the glass nat CMS 25, the sharp line observed for the sample with natural isotope distribution indicates crystallization of diopside, as confirmed by the ^{29}Si chemical shift measured.

The average ^{29}Si barycentre position for most of the ^{25}Mg enriched glasses are found in good agreement with the values given in the literature.

The chemical shift difference between enstatite ($MgSiO_3$) and diopside (CMS 25) are attributed to the differences in the degree of covalency describing the bond between silicon and the non-bridging oxygen atoms. This covalency is influenced by the cationic field strength of the alkaline-earth ions interacting with these non-bridging oxygen atoms. (43 - 44)

Table 3- Parameters for ^{29}Si MAS-NMR measured at 5.64 T. C1 and C2 stand for the components 1 and 2 in the deconvolution. δ_{iso} is the isotropic chemical shift and FWHM stands for Full Width at Half Maximum.

Samples		Barycentre \ ppm	C1	$<\delta_{iso}>$ \ ppm	*<FWHM>* \ ppm	C2	$<\delta_{iso}>$ \ ppm	*<FWHM>* \ ppm
iso	CMS 25	-83	57%	-80	14	43%	-88	20
	MAS 25	-97	52%	-88	17	48%	-106	20
	MAS 37,5	-86	57%	-81	15	43%	-91	12
	MAS 226	-92	45%	-87	25	55%	-97	17
	$MgSiO_3$	-80	100%	-80	18	-	-	-
nat	CMS 25	-86	63%	-85	1	37%	-89	2
	MAS 25	-91	56%	-87	14	44%	-96	13
	MAS 37,5	-92	51%	-86	14	49%	-98	26
	MAS 226	-91	46%	-88	17	54%	-95	18

Source: By the author

4.2 ^{27}AL MAS NMR AND TQMAS

Figure 4.3 summarizes the ^{27}Al MAS NMR spectra obtained for the central transition lineshape for the samples with enriched and natural abundance of the isotope ^{25}Mg. The best-fit ^{27}Al MAS NMR line shape parameters are listed in Table 4.

The shape of the spectra exhibit asymmetry, indicative of a broad range of quadrupolar coupling parameters. The data can be modelled by assuming the presence of

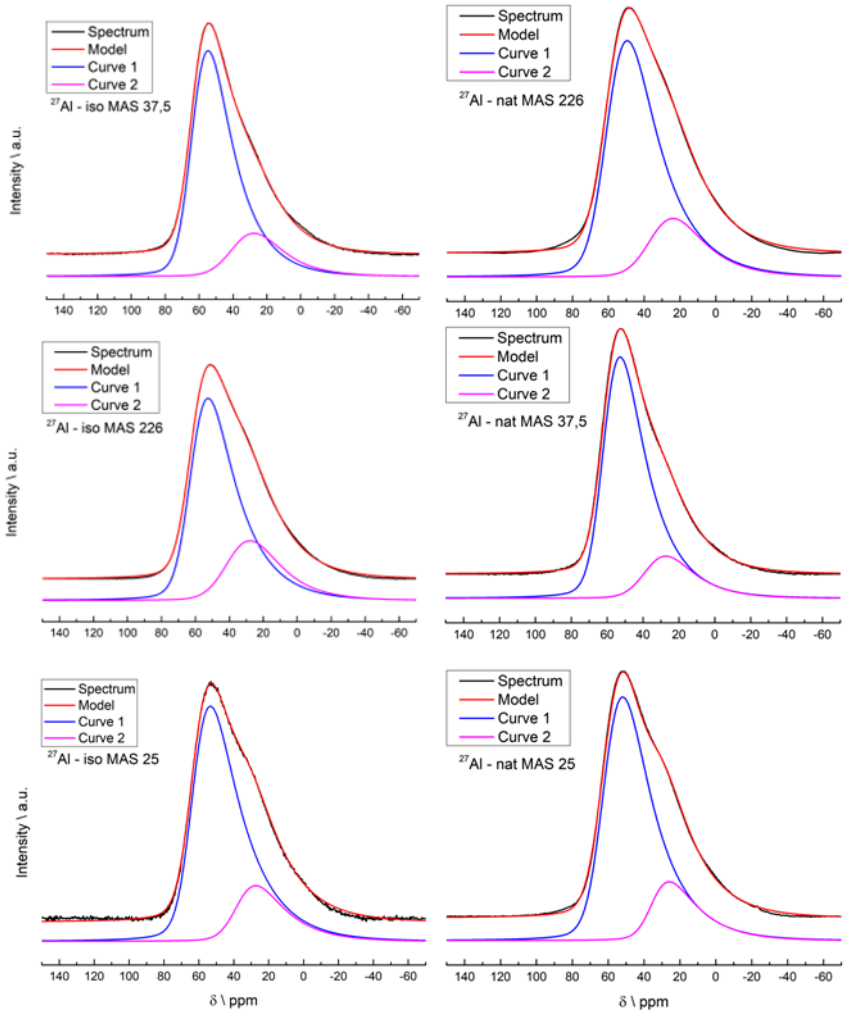

Figure 4.3 – The ^{27}Al MAS-NMR spectra were measured at 14.1 T.
Source: By the author

two separate aluminum locations, each with Czjzek line shape features and isotropic chemical shifts near 63 and 38 ppm, respectively. This would correspond to aluminum atoms that are four-coordinated and five-coordinated. (45 - 46) For the sample iso MAS 25, there is even evidence for a small fraction of six-coordinated aluminum.

Table 4 – Parameters for ^{27}Al MAS-NMR measured at 14.1 T. C1 and C2 stands for the curves 1 and 2 in the graph legends.

Samples		C1	$<\delta>$ \ ppm	$<C_Q>$ \ MHz	C2	$<\delta>$ \ ppm	$<C_Q>$ \ MHz
iso	MAS 25	81%	64	8,3	19%	38	8,1
	MAS 37,5	81%	64	7,6	19%	39	7,8
	MAS 226	75%	63	8,0	25%	40	8,0
nat	MAS 25	81%	63	8,0	19%	36	8,0
	MAS 37,5	83%	62	7,6	17%	38	7,7
	MAS 226	80%	61	8,3	20%	36	8,0

Source: By the author

To validate the existence of five-coordinated aluminum, Figure 4.4 displays exemplary SAtellite TRAnsition Spectra (SATRAS) obtained on the isotopically enriched samples. As previously mentioned, (47) the permitted $m = \pm 1/2 \leftrightarrow m = \pm 3/2$ Zeeman transitions of $I = 5/2$ nuclei are broadened by the anisotropy of the nuclear electric quadrupolar interactions. However, these transitions are only mildly affected by second-order effects, allowing magic angle spinning to transform the inhomogeneously broadened line shape into a set of sharp spinning sidebands (SSB) that are separated by multiples of the spinning frequency. Therefore, due to the absence of quadrupolar broadening effects of second order, the spectroscopic resolution of these satellite-MAS-peak patterns is superior to the resolution of the central-transition line shape, as can be seen in Figure 4.4.

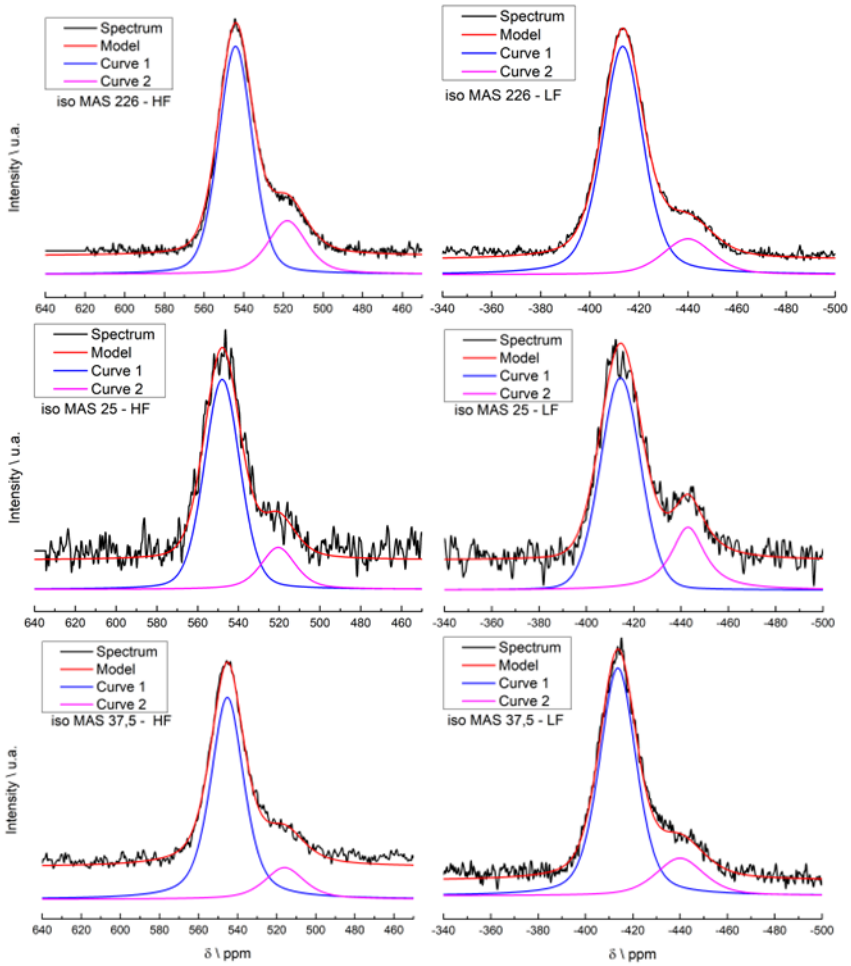

Figure 4.4 – Spectra and model of the third spinning sidebands of each the high-frequency and the low-frequency side for ^{25}Mg enriched aluminosilicate glass samples.
Source: By the author

The ^{27}Al MAS NMR data hence confirms the presence of five-coordinated Al species in all the MAS glasses examined in this study, with a proportion of the spectrum ranging from 17% to 25%. The results for the MAS 226 glass are in concurrence with prior findings (1, 48). The average coordination number n_{Al}^{O} can be calculated from the fractional areas. This information was employed in fitting neutron and x-ray diffraction data in subsequent studies (48).

Table 5 – Parameters for fitting the ^{27}Al MAS-NMR SATRAS spectra: third spinning sidebands towards high-frequency (HF) and low-frequency (LF).

Samples	HF-C1	<δ>	<FWHM>	HF-C2	<δ>	<FWHM>
MAS 25	82%	548,0	20,5	18%	520,5	20,0
MAS 37,5	84%	545,3	20,0	16%	516,0	24,0
MAS 226	77%	544,2	20,0	23%	518,0	23,0
Samples	**LF-C1**	**<δ>**	**<FWHM>**	**LF-C2**	**<δ>**	**<FWHM>**
MAS 25	74%	-414,4	20,0	26%	-443,0	17,0
MAS 37,5	81%	-413,7	19,3	19%	-440,0	24,0
MAS 226	84%	-413,4	19,5	16%	-440,0	23,8

Source: By the author

The labels LF and HF in Figure 4.4 stand for low and high frequency, respectively, while the labels C1 and C2 refer to the Czjzek lineshape components attributed to the four and five coordinate ^{27}Al.

Figure 4.5 (48) summarizes the complementary spectra measured by ^{27}Al MQMAS NMR spectra for samples with isotope ^{25}Mg natural and enriched abundance.

The spectra displayed in Figure 4.5 have been determined to possess two components, attributed to Al atoms that are 4-coordinated and 5-coordinated (plus a small amount of 6-coordinated for iso MAS 25). The average isotropic chemical shift (<δ_{iso}>) and the average second order quadrupolar effect (<*SOQE*>), as outlined in Equations (35) and (36), can be calculated and are summarized in Table 6.

For the 4-coordinated Al, the values of $\langle\delta_{\mathrm{iso}}\rangle$ and $\langle SOQE\rangle$ obtained from TQMAS NMR are in close agreement with previous studies. The diminished triple-quantum excitation efficiency observed for Al species at the higher end of the quadrupole coupling constant distribution leads to a smaller $\langle SOQE\rangle$ value from TQMAS NMR than the $\langle|C_{\mathrm{Q}}|\rangle$ values acquired from the MAS-Czjzek fits, which are considered more accurate.

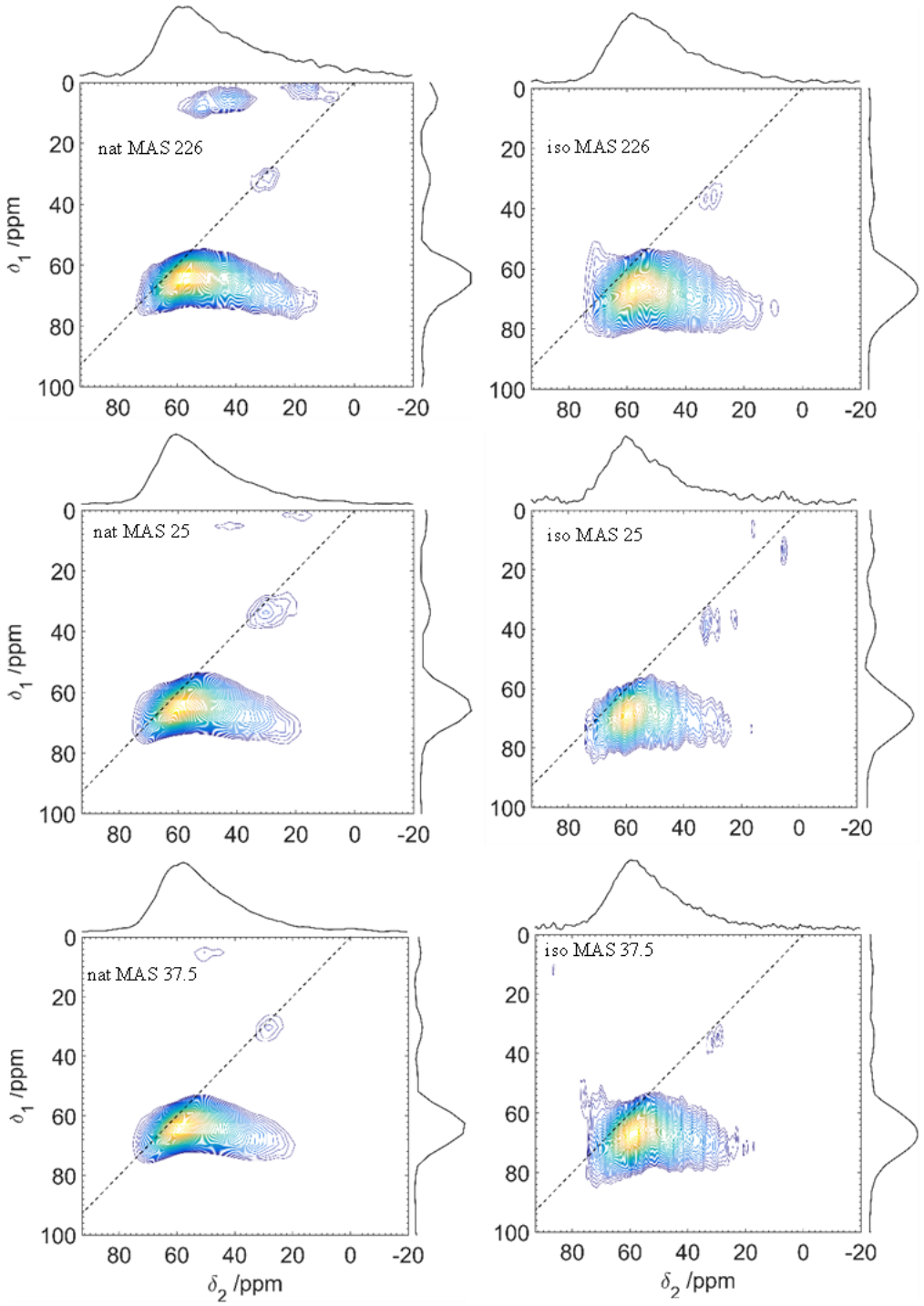

Figure 4.5- ^{27}Al MQMAS-NMR spectra at 14.1 T for isotope ^{25}Mg natural and enriched abundance samples

Source: DE OLIVEIRA. (33)

Table 6- Parameters for ^{27}Al MQMAS-NMR measured at 14.1 T. The values with indexes 1,2, and 3 refer to the 4, 5 and 6-coordinated Al, respectively.

Samples		$<\delta_{1iso}>$	$<SOQE>_1$	$<\delta_{2iso}>$	$<SOQE>_2$	$<\delta_{3iso}>$	$<SOQE>_3$
iso	MAS 25	63	6.1	36	4,7	11	4.6
	MAS 37,5	63	6,1	36	4.7	-	-
	MAS 226	61	6,2	35	3,5	-	-
nat	MAS 25	59	7,1	31	2.9	-	-
	MAS 37,5	60	5,7	31	3.2	-	-
	MAS 226	60	6,1	31	3,7	-	-

Source: By the author

For the 5-coordinated Al, the ⟨*SOQE*⟩ values are notably underestimated by TQMAS, which can be attributed to the low signal-to-noise ratio.

For the iso MAS 25 sample, a small peak at δ_3 from 0 to 20 ppm in the TQMAS spectrum suggests a slight presence of 6-coordinated Al, which was also confirmed by the MAS NMR spectrum analysis.

It is possible that we have overestimated the amount of Al(VI) listed in Table 6. This is because the presence of Al(VI) is not clear from the SATRAS data for this sample in Figure 4.4. In general, for a given composition, the interaction parameters obtained from the ^{27}Al NMR spectra measured for the isotopically enriched ^{25}Mg glasses vs those measured for the glasses with the natural isotopic abundance distribution are similar, within some experimental errors.

4.3 ^{25}Mg ROTOR SYNCHRONIZED HAHN SPIN ECHO (RHE)

By analyzing the data obtained from MAS-NMR, we can glean valuable information about the internal interactions that influence the Zeeman levels of ^{25}Mg nuclei. However, due to the presence of significant probe ringing at low resonance frequencies, the most effective method for obtaining high-quality MAS-NMR line shapes is through the measurement of rotor-synchronized MAS echoes.

The resulting spectra and their deconvolutions are illustrated in Figure 4.6. A similar line shape was found for all the isotopically enriched samples measured. This line shape is indicative of a wide distribution of quadrupolar coupling strengths, creating a wide and asymmetric dispersion. Despite the intensity of the quadrupolar coupling strengths, their effects on the NMR line shape can be treated under the regime of second-order perturbation theory, as discussed in Section 2.2.3. The spectra were obtained at a rotor frequency of 20.0 kHz (acquisition after two rotor cycles). The spectra are in black

curves, and the simulations obtained from a distribution of electric field gradients modeled using the Czjzek distribution are shown by red curves.

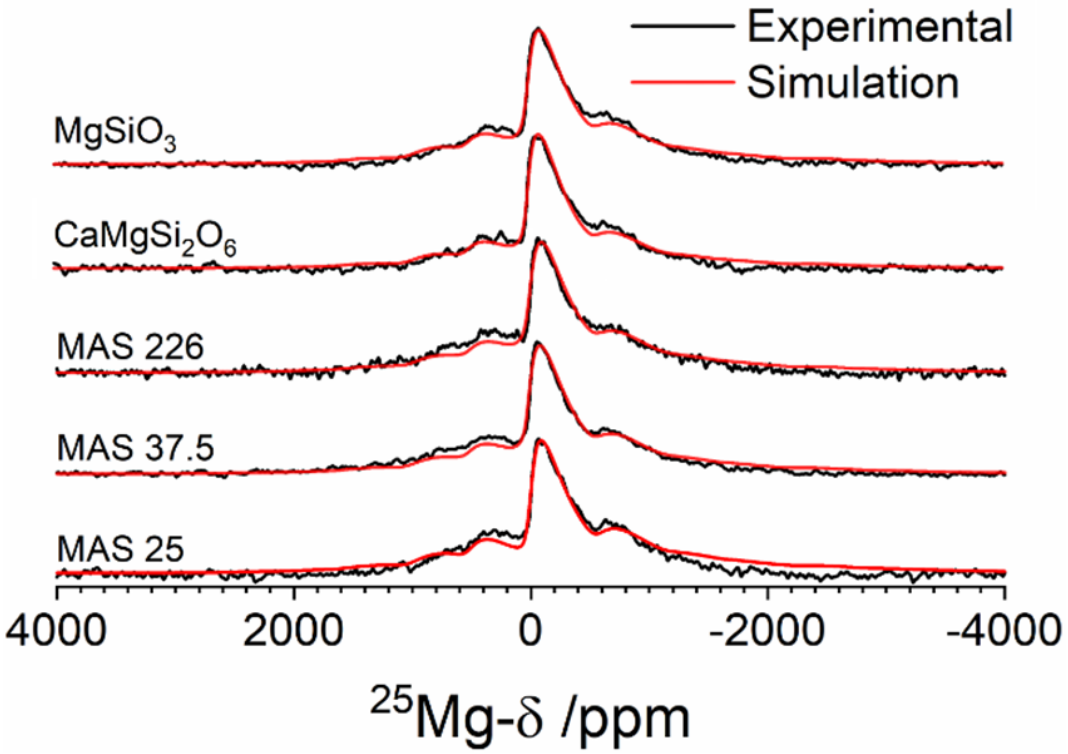

Figure 4.6 - ^{25}Mg MAS NMR spectra obtained through rotor-synchronized Hahn spin echo. Source: DE OLIVEIRA. (33)

We were able to successfully model the overall shape by utilizing a Czjzek distribution within the ssNake program, as outlined in the literature (36). The simulations were performed assuming a finite MAS rate regime, and by utilizing the Carousel averaging approach implemented in the software, 16 spinning sidebands were included in the simulation. Additionally, an approach with unrestricted parameters was utilized, leading to the identification of the best fit parameters through interactions. To account for a distribution of isotropic chemical shifts, a Gaussian line-broadening (LB) parameter was also employed.

The results of these simulations are listed in Table 7. The Czjzek model was used as implemented in the ssNake software with the fitting parameters not restricted.

The mean chemical shift was found to be in the range of 12 to 28 ppm, however, due to the large linewidth found in the spectra, there may be some inaccuracies in this value. It is typical for crystalline compounds to have a chemical shift in the range of zero to 30 ppm relative to an aqueous $MgCl_2$ solution, when magnesium is present in a 6-coordinated environment (Mg(VI)), while a chemical shift in the range of 40–80 ppm is

typically attributed to magnesium in a 4-coordinated environment (Mg(IV)) (49). Therefore, the results suggest that the Mg^{2+} ions in the different glasses are primarily 6-coordinated.

Table 7 – Deconvolution analysis of the central transition of the ^{25}Mg MAS NMR spectra of the glass samples under study.

Sample	$<\delta_{iso}>$ (±5 ppm)	σ (±0.2 MHz)	$<\|C_Q\|>$ (±0.4 MHz)	*LB* (±0.5 kHz)
CMS 25	13	4.2	8.3	2.0
MgSiO3	13	4.4	8.6	3.0
MAS 37.5	28	4.5	8.9	2.5
MAS 25	12	4.5	8.9	3.0
MAS 226	20	4.5	8.9	2.5

Source: By the author

By using MAS-NMR, the resonance signals of those nuclei that are at the low end of the C_Q distribution (up to a limiting value of C_{Qmax}) show significantly narrowed spectra, while the second-order perturbative nature of these interactions still confers anisotropic line broadening effect to the lineshape that persists, and which increase proportionally with increasing C_Q values. On the one hand, signals of the resonance on those nuclei which are affected by strong quadrupolar coupling at the high end of the distribution of C_Q values are unaffected (or little affected) by the MAS sample rotation, which contributes to the broad part of the spectrum. Furthermore, the ratio of the spinning frequency to the quadrupolar frequency has an influence on the ability of MAS-NMR to provide an effective lineshape narrowing.

By using MAS-NMR is important to have in mind that the increasing of the spinning speed is also responsible for shifting the limit of C_{Qmax} towards higher values, which implies proportionally more nuclei with higher degrees of distortions in their immediate electronic environments (and therefore broader NMR signals) contribute to the narrower characteristic of the MAS-NMR line shape. As a result, this set of nuclei includes more and more nuclei with increasingly distorted environments as the rotation frequency increases, resulting in an increased linewidth with increasing spinning speed. This effect will always occur if the distribution of quadrupole coupling constants is so wide that only part of the whole set can be effectively narrowed by MAS-NMR.

Equally important, if there is an absence of a spinning speed dependence of the MAS-NMR spectra on the MAS spinning frequency this would signify that all nuclei present in the sample contribute to the narrow MAS NMR line shape. In the present case,

our results indicate that magnetic field strengths higher than 14.1 T and/or spinning frequencies higher than 24 kHz would be required to reach such a situation. Therefore, we suspect that many of the reported values of $<|C_Q|>$ for ^{25}Mg in the literature for glasses containing magnesium of natural isotopic abundance and measured under similar conditions may be under-estimated. Likewise, the $<\delta_{iso}>$ values reported for ^{25}Mg in glasses may not be representative because they only refer to a sub-set of nuclei interacting with weaker EFGs, which contribute to the narrower lineshape feature.

In Figure 4.7, a left shifting was applied in the time domain to eliminate the signal acquired during the first 24μs of the acquisition time prior to Fourier transformation. This removes the rapidly decaying part of the FID, leading to an artificial flattening of the baseline following a first-order phase correction. Values found for $<|C_Q|>$ and $<\delta_{iso}>$ using the Czjzek model (red curves in Figure 4.7) are displayed in Table 8.

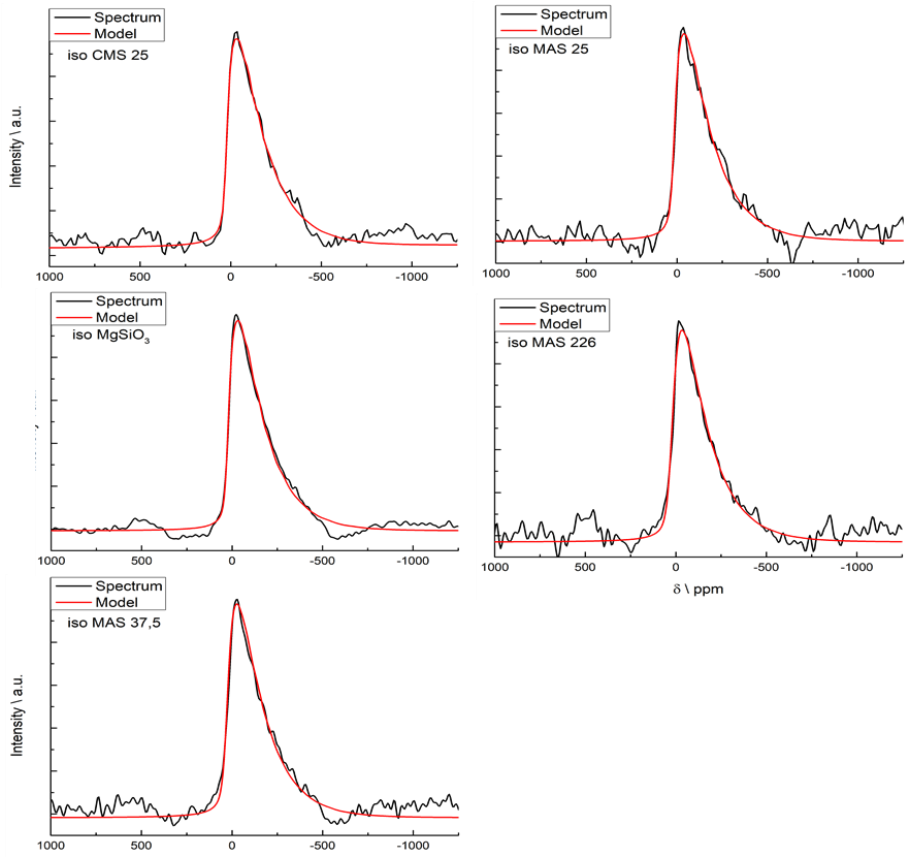

Figure 4.7- ^{25}Mg RS-HSE - NMR spectra at 14.1 T for ^{25}Mg enriched abundance samples. Fourier transforms obtained after left shifting the data acquired within a 24 μs range from the trailing part of the echo prior to Fourier transformation. The red curve shows a simulation based on the Czjzek model using the DMfit software.

Source: By the author

The values found using this approach lead to some discrepancies compared to those listed in Table 7, both with respect to $<\delta_{iso}>$ and $<|C_Q|>$. In particular, the $<|C_Q|>$ values are significantly underestimated by left-shifting the data. Thus, this method must be considered unreliable.

Table 8 - Parameters found for the modeling process using DMfit with the Czjzek after left shifting the data acquired within a 24 μs range from the trailing part of the echo prior to Fourier transformation.

Samples	$<\delta_{iso}>$ \ ppm	$<C_Q>$ \ MHz
iso CMS 25	27	5,7
iso MAS 25	20	5,6
iso MAS 37,5	27	5,3
iso MAS 226	26	5,5
iso $MgSiO_3$	26	5,5

Source: By the author

4.4 ^{25}Mg WURST-CMPG – NMR

The WURST-CPMG technique was applied on static samples CMS 25 and $MgSiO_3$. To analyze the static lineshapes including the satellite transitions, the measurement was done at various resonance offsets. Figure 4.8 presents the spectra obtained, and the red arrows indicate the position where the pulses were centred for each part of the experiment. The spectra displayed the characteristic asymmetry typical of quadrupolar nuclei under the influence of strong electric field gradients, thus requiring the application of second-order perturbation theory for their description. The broad distribution of quadrupolar coupling strengths, as seen in the spectra, reflects the inherent disorder present in the glassy state. The central transition lineshape was observed to be affected by limited probe bandwidth when measured at different resonance offsets. Nevertheless, the results suggest that these distortions can be disregarded when the frequency carrier is placed at the maximum of the lineshape, allowing for the modelling without the need to consider off-resonance distortions.

Figure 4.9 shows a simulation of the ^{25}Mg static NMR spectra using the Czjzek model. The red arrows indicate the resonance offsets used for the stepwise acquisition of the wideline spectra. The model successfully reproduces the asymmetric lineshapes

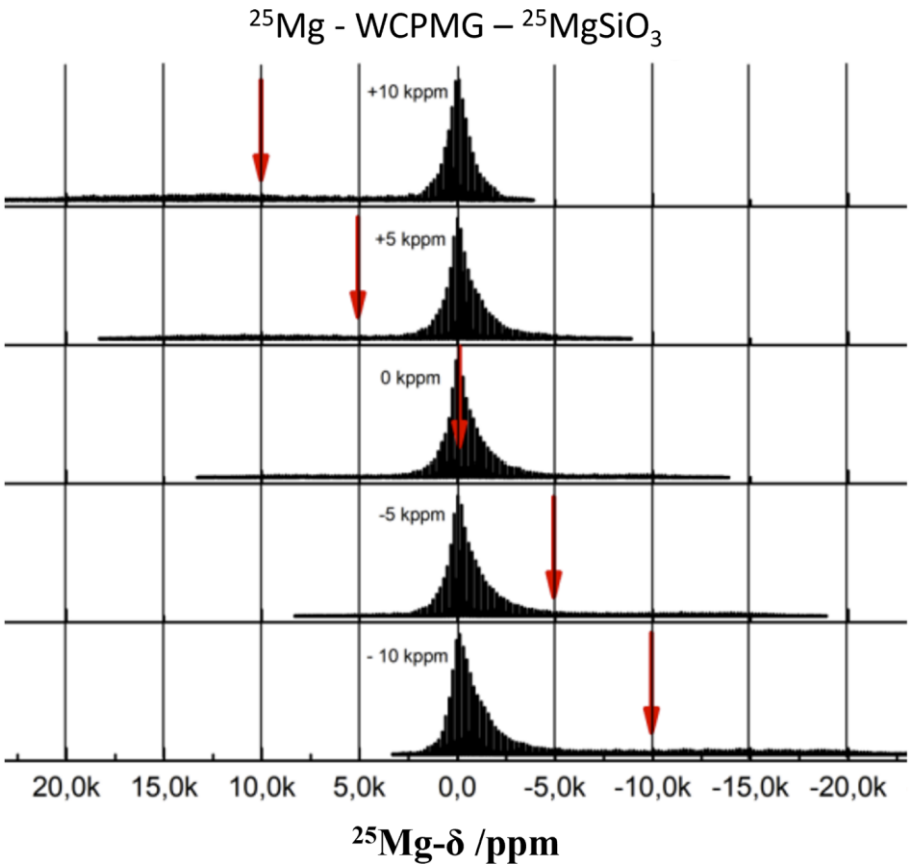

Figure 4.8 - Static ^{25}Mg WURST-CPMG spikelet spectra obtained on $MgSiO_3$ glass
Source: DE OLIVEIRA. (33)

measured under static conditions, using widths for the Czjzek distributions (σ) of 4.4 and 4.2 MHz, corresponding to average magnitude values $\langle|C_Q|\rangle$ of 8.6 and 8.3 MHz for the $MgSiO_3$ and $CaMgSi_2O_6$ samples, respectively. The average isotropic chemical shift was estimated at 13 ppm. The optimization of the simulations was done to find a single set of parameters for each sample that reproduces both the static and the M AS spectra.

The simulations displayed in (33) were obtained by using the parameters obtained from the simulations of the MAS spectra (Figure 4.6). The arrows in the figure indicate the resonance offsets used for the stepwise acquisition of the wideline spectra. The Czjzek model can reproduce the asymmetric lineshapes of the static spectra, providing further evidence of its ability to describe the quadrupolar interaction in the glassy samples.

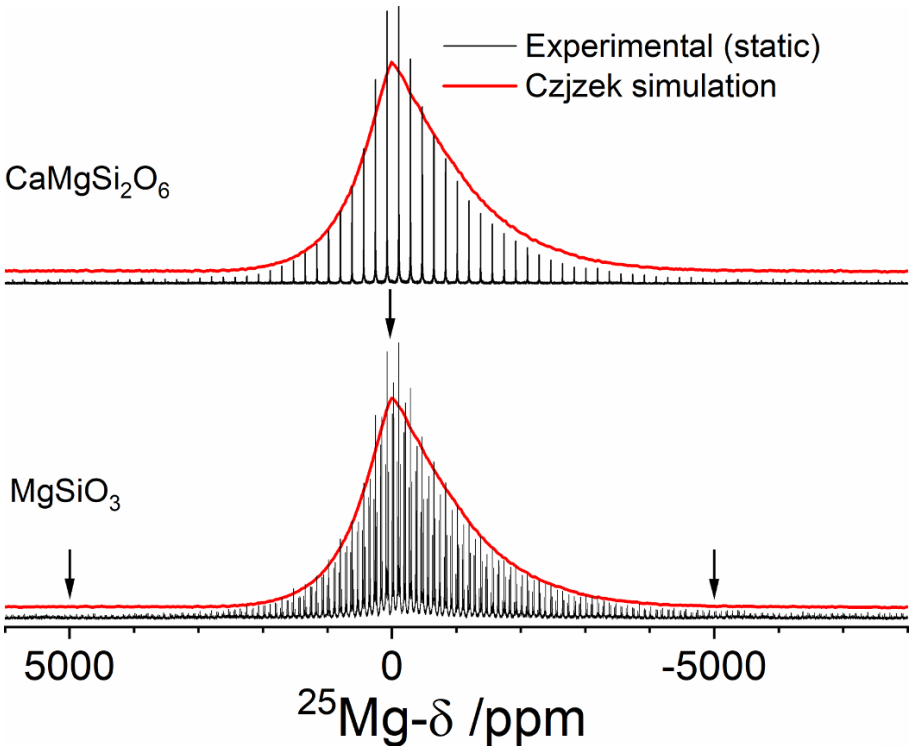

Figure 4.9 - Static 25Mg WURST-CPMG spikelet spectra for both enstatite, MgSiO3 and diopside, CMS 25, glasses, as well as the Czjzek distribution simulations.
Source: DE OLIVEIRA. (33)

Figure 4.10 (33) shows the experimental and simulated static spectra over their full-scale range. Part (a) presents the complete static frequency spectrum for both the $MgSiO_3$ and CMS 25 glass samples, accompanied by model simulations that utilize EFG distributions that adhere to the Czjzek model, and (b) presents a heightened focus on the vertical expansion, particularly the quadrupolar satellite spikelets. The arrows indicate the specific resonance offsets utilized for the stepped acquisition of the broad line spectra. Distinctive spikelet patterns are clearly visible to both sides of the central resonance, which can be attributed to the satellite transition manifold. Also included are the

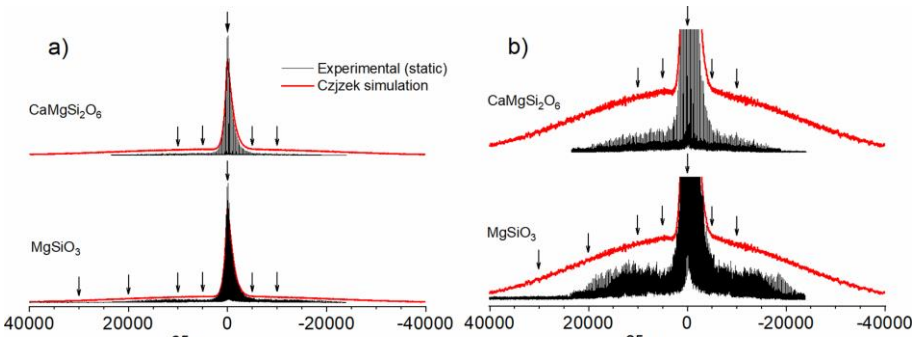

Figure 4.10 - Detailed WURST spectra of enstatite and diopside glass over the full spectral range.
Source: DE OLIVEIRA. (33)

simulated spectra (red curves). While the frequency range of the satellite spectra is well-consistent with the information obtained from the central transition spectra discussed above, the intensity of the satellite transitions appears diminished. We suspect that the deviation between simulated and experimental spectra may arise from a less efficient excitation of satellite transitions by the WURST pulses.

4.5 ^{25}Mg STATIC SPIN ECHO DECAY SPECTROSCOPY

Previous studies have shown that Hahn spin echo decay spectroscopy can effectively measure the strength of homonuclear magnetic dipole-dipole interactions in nuclei with spin-3/2 and spin-5/2 by selectively exciting the central transition m = ½ ↔ m = - ½. This technique has been commonly applied in investigating the spatial distribution of sodium ions in oxide glasses. (50)

Figure 4.11 examines this approach in relation to a measurement of the ^{25}Mg-^{25}Mg dipole-dipole interactions in isotopically enriched materials. The graphs present two different experiments that correspond to nutation frequencies of 25 kHz (black triangles) and 80 kHz (red circles). As shown in Figure 4.11, the results are consistent within experimental error, which suggests that the central transition is selectively excited under both conditions. For the diopside glass, data is also shown for a sample with magnesium of natural isotopic abundance (blue open stars, right). Because of the long times necessary for the signal accumulation to reach acceptable signal-to-noise ratios, the limited signal to noise ratios obtained with the natural abundance samples, only a few dipolar evolution times were studied.

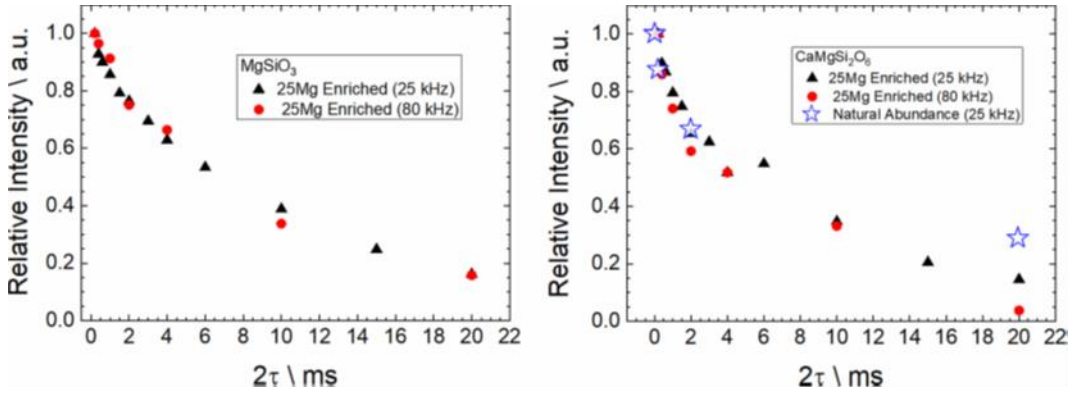

Figure 4.11 - ^{25}Mg spin echo decay of (left) $MgSiO_3$ glass and (right) CMS 25 glass at two radiofrequency power levels.

Source: DE OLIVEIRA. (33)

The results indicate that the spin echo signal of diopside glass decays slightly faster than that of $MgSiO_3$ glass, particularly at shorter evolution times ($2\tau < 2$ ms). This outcome is unexpected as the total ^{25}Mg concentration in enstatite glass is twice as high as in diopside glass. It is likely that, even in the isotopically enriched materials, the dipole-dipole coupling is so weak that the nuclear electric quadrupolar interaction dominates the spin echo decay response. This conclusion is supported by additional experiments, which show that the echo decay rate in the magnetically diluted samples at natural abundance (10% ^{25}Mg) is similar to that measured for the isotopically enriched material. Therefore, we conclude that even in the isotopically enriched materials, the homonuclear interactions are too weak to be measured by the simple spin echo decay method. More advanced techniques such as double quantum excitation may have to be used.

5 CONCLUSION AND PERSPECTIVES

In the present work we were able to employ several techniques of Solid-State NMR in order to study the structure of magnesium alumino and aluminosilicate glasses.

For ^{29}Si, we employed MAS NMR spectroscopy, but due to limitations in the amount of material available and long spin-lattice relaxation times, reliable signal deconvolution in terms of the contributions from different Q^n units could not be obtained. However, the spectra were found to be consistent with previously published data. Additionally, the study found that the average isotropic chemical shifts and full widths at half maximum were found to be identical for the samples with and without ^{25}Mg isotopic enrichment for MAS 226 glass, but there were stronger deviations for the other compositions, which are attributed to the relatively large experimental error caused by the low signal-to-noise ratio. It was still possible to simplify the spectrum by using two components giving similar values for the barycenter of the spectra as the usual from four components.

For ^{27}Al, the data from MAS-NMR on the samples suggests the presence of two distinct aluminum coordination environments in the samples. The results also show that there is evidence for a small fraction of six-coordinated aluminum in the sample iso MAS 25. We further employed complementary techniques such as ^{27}Al MQMAS NMR spectra and SATRAS-NMR to further validate the findings.

^{25}Mg spectra obtained via a rotor-synchronized MAS spin echo sequence were simulated using a Czjzek distribution within the ssNake program. They suggest that the Mg^{2+} ions in the different glasses are primarily 6-coordinated. There were some limitations of MAS-NMR, including the effects of spinning speed on the MAS-NMR spectra and the limitations of the $<\delta_{iso}>$ values reported for ^{25}Mg in glasses. A commonplace method involving left shifting the data in the time domain, which eliminates the broad feature from the spectra was shown to lead to unacceptable distortions. Czjzek fits to such artificially treated spectra tend to underestimate C_Q-values but did not affect the conclusions reached on the basis of the isotropic chemical shifts extracted from the data.

The WURST-CPMG technique applied to static samples of ^{25}Mg enriched CMS 25 and $MgSiO_3$ resulted in NMR spectra that showed the characteristic asymmetry of

quadrupolar nuclei under the influence of strong electric field gradients with a wide distribution, and were successfully analysed using the Czjzek model. The simulation was optimized to find a single set of parameters for each sample that reproduces both the static and the MAS spectra. However, the experimental spectra showed reduced intensity of the satellite transition spikelets in comparison to the simulations, which may be due to less efficient excitation of satellite transitions by the WURST pulses.

On what concerns to the Hahn spin echo decay of ^{25}Mg nuclei, the present study indicates that a measurement of the ^{25}Mg-^{25}Mg dipole-dipole interactions in isotopically enriched materials. The result may be explained considering that the dipole-dipole coupling is too weak to dominate the spin echo decay. Rather the spin echo decay is dominated by the nuclear electric quadrupolar interaction. Advanced techniques such as double quantum excitation may have to be used for the selective measurement of ^{25}Mg-^{25}Mg dipole-dipole coupling in glasses.

REFERENCES

1 BRADTMÜLLER, H. *et a*l. Structural origins of crack resistance on magnesium aluminoborosilicate glasses studied by solid-state NMR. **Journal of Physical Chemistry C**, v. 123, n. 24, p. 14941–14954, June 2019.

2 MOGHANIAN, A. *et al*. Novel antibacterial Cu/Mg-substituted ^{58}S-bioglass: synthesis, characterization and investigation of in vitro bioactivity. **International Journal of Applied Glass Science,** v.11, n.4, p. 685–698, Oct.2020.

3 TABIRA, Y. Local structure around oxygen atoms in $CaMgSi2O_6$ glass by O K-edge EXELFS. **Materials Science and Engineering B**, v. 41, n. 1, p. 63–66, Oct. 1996.

4 WILDING, M. C.; BENMORE, J. A.; TANGEMAN, C. J.; SAMPATH, S. "Evidence of different structures in magnesium silicate liquids: coordination changes in forsterite- to enstatite-composition glasses", **Chemical Geology**, v. 213, n. 1, p. 281–291, Dec. 2004.DOIi: 10.1016/j.chemgeo.2004.08.055.

5 ILDEFONSE, P.H. *et al.* Low Z elements (Mg, Al, and Si) K-edge X-ray absorption spectroscopy in minerals and disordered systems. **Nuclear Instruments and Methods in Physics Research B**, v. 97, p. 172–175, May 1995.

6 ROEKER, S.; STEBBINS, J. F. Magnesium coordination environments in glasses and minerals: new insight from high-field magnesium-25 MAS NMR. **American Mineralogist**, v. 85, n. 10, p. 1459–1464, Oct. 2000.

7 RAO, K. J. **Structural chemistry of glasses**. Amsterdam: Elsevier, 2017.

8 ZACHARIASEN,W. H. The atomic arrangement in glass**, Journal of American Chemical Society**, v. 54, n. 10, p. 3841–3851, Oct.1932, DOI: 10.1021/ja01349a006.

9 GREAVES, G. N. EXAFS and the structure of glass. **Journal of Non-Crystalline Solids:** effects of modes of formation on the structure of glass, v. 71, n. 1, p. 203–217, May 1985.

10 ZANOTTO,E. D.; MAURO, J. C. The glassy state of matter: its definition and ultimate fate, **Journal of Non-Crystalline Solids**, v.471, p.490–495, Sept.2017. DOI: 16/j.jnoncrysol.2017.05.019.

11 CONRADT. Thermodynamics of glasses. *In*: AKIRA, Takada. **Teaching glass better**. Madrid: ICG, 2019. p. 153–173.

12 MAURO, J. C.; LOUCKS, R. J.; GUPTA, P. K. Fictive temperature and the glassy state**. Journal of the American Ceramic Society**, v.92, n.1, p. 75–86, Jan. 2009.

13 VARSHNEYA, A. K. Fundamentals of the glassy state. In: VARSHNEYA, A. K. **Fundamentals of inorganic glasses**. San Diego (USA): Academic Press, 1994. chap. 2, p. 13–25.

14 BRAGG, W. The glassy state. *In*: RAO, K. J. (ed.). **Structural chemistry of glasses**. Oxford: Elsevier Science Ltd, 2002. chap.2. p. 13–76.

15 ABRAGAM, A. **Principles of nuclear magnetism**. New York (USA): Oxford University Press, 1983.

16 CZJZEK, G. *et al*. Atomic coordination and the distribution of electric field gradients in amorphous solids. **Physical Review B**, v. 23, n. 6, p. 2513–2530, Mar. 1981.

17 D'ESPINOSE DE LACAILLERIE, J.B.; FRETIGNY, C.; MASSIOT, D. MAS NMR spectra of quadrupolar nuclei in disordered solids: the Czjzek model. **Journal of Magnetic Resonance,** v.192,n.2, p.244-251**,** June 2008.

18 HAHN, E. L. Nuclear induction due to free larmor precession. **Physical Review**, v. 77, n. 2, p. 297–298, Jan. 1950.

19 CARR, H. Y.; PURCELL, E. M. Effects of diffusion on free precession in nuclear magnetic resonance experiments. **Physical Review**, v. 94, n. 3, p. 630–638, May 1954.

20 MEIBOOM, S.; GILL, D. Modified spin-echo method for measuring nuclear relaxation times. **Review of Scientific Instruments**, v. 29, n. 8, p. 688–691, Aug.1958.

21 LARSEN, F. H. *et al*. High-field QCPMG-MAS NMR of half-integer quadrupolar nuclei with large quadrupole couplings. **Molecular Physics**, v. 95, n. 6, p. 1185–1195, Dec. 1998.

22 O'DELL, L. A. The WURST kind of pulses in solid-state NMR. **Solid State Nuclear Magnetic Resonance**, v. 55–56, p. 28–41, 2013.

23 ANDREW, E. R.; BRADBURY, A.; EADES, R. G. Removal of dipolar broadening of nuclear magnetic resonance spectra of solids by specimen rotation. **Nature**, v. 183, p. 1802–1803, June 1959.

24 LOWE, I. J. Free induction decays of rotating solids. **Physical Review Letters**, v. 2, n. 7, p. 285–287, April 1959.

25 DUER, M. J. **Introduction to solid-state NMR spectroscopy**. Cambridge (UK): Wiley-Blackwell, 2005.

26 SAMOSON, A.; LIPPMAA, E. Excitation phenomena and line intensities in high-resolution NMR powder spectra of half-integer quadrupolar nuclei. **Physical Review B**, v. 28, n. 11, p. 6567–6570, Dec.1983.

27 BALTISBERGER, J. H. *et al*. Triple-quantum two-dimensional ^{27}Al magic-angle spinning nuclear magnetic resonance spectroscopic study of aluminosilicate and aluminate crystals and glasses. **Journal of the American Chemical Society**, v. 118, n. 30, p. 7209–7214, Jan. 1996.

28 DUER, M. J. **Solid state NMR spectroscopy:** principles and applications. Cambridge (UK): John Wiley & Sons, 2008.

29 AMOUREUX, J. P.; FERNANDEZ, C.; STEUERNAGEL, S. Z. Filtering in MQMAS NMR. **Journal of Magnetic Resonance,** v.123, n.1, p. 116–118, Nov. 1996.

30 AMOUREUX, J. P.; HUGUENARD, C.; ENGELKE, F. Unified representation of MQMAS and STMAS NMR of half-integer quadrupolar nuclei. **Chemical Physics Letters**, v. 356, n. 5, p. 497–504, 2002.

31 CORMIER, L.; CUELLO, G. J. Mg coordination in a $MgSiO_3$ glass using neutron diffraction coupled with isotopic substitution. **Physical Review B**, v. 83, n. 22, p. 224204, June 2011.

32 CORMIER, L.; CUELLO, G. J. Structural investigation of glasses along the $MgSiO_3$–$CaSiO_3$ join diffraction studies. **Geochimica et Cosmochimica Acta**, v. 122, p. 498–510, Dec. 2013

33 DE OLIVEIRA, M. *et al*. Analysis and information content of quadrupolar NMR in glasses: ^{25}Mg NMR in vitreous $MgSiO_3$ and $CaMgSi_2O_6$. **Journal of Magnetic Resonance Open**, v. 12–13, p. 100067, Dec. 2022.

34 MASSIOT, D. *et al.* Modelling one- and two-dimensional solid-state NMR spectra**. Magnetic Resonance in Chemistry**, v. 40, n. 1, p. 70–76, 2002.

35 FREUDE, D.; HAASE, J. Quadrupole effects in solid-state nuclear magnetic resonance. *In*: PFEIFER, H., BARKER, P. (ed.). **Special applications**: NMR basic principles and progress, Berlin: Springer,1993. v.29.

36 VAN MEERTEN, S. G. J.; FRANSSEN, W. M. J.; KENTGENS, A. P. M. ssNake: A crossplatform open-source NMR data processing and fitting application. **Journal of Magnetic Resonance**, v. 301, p. 56–66, Apr. 2019.

37 BAK, M.; RASMUSSEN, J. T.; NIELSEN, N. C. SIMPSON: a general simulation program for solid-state NMR spectroscopy. **Journal of Magnetic Resonance**, v. 147, n. 2, p. 296–330, Dec. 2000.

38 FRASER, D. G.; CLAYDEN, N. J. A high-resolution ^{29}Si nuclear magnetic resonance study of ordering in silicate glasses on the join $CaMgSi_2O_6NaAlSi_3O_8$. **Chemical Geology**, v. 62, n. 1, p. 43–47, April 1987.

39 GAUDIO, S. J.; SEN, S.; LESHER, C. E. Pressure-induced structural changes and densification of vitreous $MgSiO_3$. **Geochimica et Cosmochimica Acta**, v. 72, n. 4, p. 1222–1230, Feb. 2008.

40 IBOUREL, G. *et al*. ^{29}Si and ^{27}Al MAS-NMR spectroscopy of glasses in the system $CaSiO_3$-$MgSiO_3$-Al_2O_3. **Chemical Geology**, v. 96, n. 3, p. 387–397, April 1992.

41 SCHNEIDER, J. *et al.* ^{29}Si MAS–NMR studies of Q^n structural units in metasilicate glasses and their nucleating ability. **Journal of Non-Crystalline Solids**, v. 273, n. 1–3, p. 8–18, Aug.2000.

42 SCHNEIDER, J. *et al*. Q^n distribution in stoichiometric silicate glasses: thermodynamic calculations and ^{29}Si high resolution NMR measurements. **Journal of Non-Crystalline Solids**, v. 325, n. 1, p. 164–178, Sept. 2003.

43 LOGRADO, M. *et al.* Structure-property relations in crack-resistant alkaline-earth aluminoborosilicate glasses studied by solid state NMR**. Journal American Ceramic Society,** v.104, n.5, p.2250-2267, May 2021.

44 MURDOCH, J. B.; STEBBINS, J. F.; CARMICHAEL, I. S. E. High-resolution ^{29}Si NMR study of silicate and aluminosilicate glasses: the effect of network-modifying cations. **American Mineralogist,** v. 70, n. 3–4, p. 332–343, April 1985.

45 ECKERT, H. Structural studies of noncrystalline solids using solid state NMR: new experimental approaches and results*. In:* BLUMICH, B. *et al*. **Solid-state NMR IV methods and applications of solid-state NMR**: basic principles and progress. Berlin, Heidelberg: Springer, 1994. v. 33p. 125–198.

46 EDÉN, M. ^{27}Al NMR studies of aluminosilicate glasses*. In*: WEBB, G. A. (ed.). **Annual reports on NMR spectroscopy**. New York*;* Academic Press, 2015. v. 86, p. 237–331.

47 JÄGER, C. *et al.* ^{27}Al MAS-NMR spectroscopy of glasses: new facilities by application of 'SATRAS'. **Journal of Non-Crystalline Solids**, v. 149, n. 3, p. 209–217, Nov. 1992.

48 MOHAMMADI, H. *et al.* Structure of diopside, enstatite, and magnesium aluminosilicate glasses: A joint approach using neutron and x-ray diffraction and solid-state NMR. **Journal of Chemical Physics**, v. 157, n.21, p.214503, 2022.

49 FREITAS, J. C. C.; SMITH, M. E. Recent advances in solid-state ^{25}Mg NMR spectroscopy. *In:* WEBB, G. A. (Ed.). **Annual reports on NMR spectroscopy**. New York*:* Academic Press, 2012. v. 75, chap. 2, p. 25–114.

50 ECKERT, H. Short and medium range order in ion-conducting glasses studied by modern solid state NMR techniques. **Zeitschrift für Physikalische Chemie**, v. 224, n. 10–12, p. 1591–1654, Nov. 2010.